Lattice Boltzmann modelling of streaming potentials: variations with salinity in monophasic conditions

Eve-Agnès Fiorentino, Renaud Toussaint, Laurence Jouniaux

Geophysical Journal International

Geophys. J. Int. (2016) **205,** 648–664
Advance Access publication 2016 January 29
GJI Marine geosciences and applied geophysics

doi: 10.1093/gji/ggw041

Lattice Boltzmann modelling of streaming potentials: variations with salinity in monophasic conditions

Eve-Agnès Fiorentino, Renaud Toussaint and Laurence Jouniaux

Institut de Physique du Globe de Strasbourg, CNRS/UMR 7516*, University of Strasbourg, Strasbourg, France. E-mail: eafiorentino@unistra.fr*

Accepted 2016 January 22. Received 2015 December 15; in original form 2015 June 25

SUMMARY

The streaming potential phenomenon is produced by the flow of an electrolyte in a porous medium and is used for geophysical prospecting. It is quantified through an electrokinetic (EK) coefficient. The dependence of the EK coefficient on the conductivity of the electrolyte is described by the Helmholtz–Smoluchowski (HS) equation. This equation provides successful forecasts of the EK coefficient in the standard range of concentration. However, experimental measurements show deviations to this equation at extreme low and extreme high salinities. The aim of this study is to model the EK coefficient using Lattice Boltzmann simulations in a 2-D capillary channel, with a view to understanding these deviations. The effect of the constitutive parameters of the HS equation such as the permittivity and the viscosity is discussed. The validity of the HS equation using strong ζ potentials is assessed. Finally, a model of bulk fluid conductivity is derived. This model allows to take into account the change of local ionic distribution in the vicinity of the mineral. It appears to have a significant impact on the derivation of ζ potentials at low salinities and in the presence of polyvalent counterions.

Key words: Numerical solutions; Electrical properties; Hydrogeophysics.

1 INTRODUCTION

The streaming potential phenomenon is induced by the coupling between the fluid flow and the electrical flow, which results from the presence of an electrical double layer at the fluid-rock interface. When fluid flows through a porous medium, it gives rise to an electric streaming current, counterbalanced by a conduction current, leading to a measurable electrical voltage. This electrokinetic effect is at the origin of seismoelectric signals (Gao & Hu 2010; Gao *et al.* 2013; Warden *et al.* 2013; Zyserman *et al.* 2015) and self-potential (SP) signals. Surface observations of SP anomalies have been reported from numerous tectonically active areas in the world, at different scales from centimetric to kilometric, at the Earth surface or in boreholes. The SP method has been used to characterize active volcanic areas (Saracco *et al.* 2004; Mauri *et al.* 2010) to detect at distance the propagation of a water-front in a reservoir (Saunders *et al.* 2008) and used to map ground water flow features (Jouniaux *et al.* 1999; Sailhac & Marquis 2001). It is possible to quantify this streaming potential with laboratory measurements (Jouniaux *et al.* 1994; Maineult *et al.* 2006; Jaafar *et al.* 2009; Glover & Déry 2010; Vinogradov *et al.* 2010; Vinogradov & Jackson 2011; Wang & Hu 2012).

The electrical double layer stems from the charge of the minerals constituting the material in contact with the electrolyte. When an electrolyte flows in a rock channel, the local electroneutrality in the immediate vicinity of the surface is satisfied thanks to an excess of positive ions, adsorbed and immobile, forming the Stern layer. The amount of positive ions decays as getting away from the mineral, until both positive and negative ions are found in equal proportion, in the free neutral part, far from the surface. The transition between the Stern layer and the free neutral electrolyte is called the diffuse layer. The so-called electrical double layer (EDL) is the combination of the Stern and the diffuse layers.

The potential created by the ionic distribution is related to the charge density of the electrolyte through the Poisson–Boltzmann equation:

$$\Delta\psi = -\sum_i \frac{z_i e C_i^{\infty}}{\varepsilon_r \varepsilon_0} \exp\left(-\frac{z_i e \psi}{k_B T}\right) \tag{1}$$

where n is the number of species, $\varepsilon_0 = 8.85 \times 10^{-12}$ F m^{-1} is the vacuum permittivity, ε_r is the relative permittivity of water, $e = 1.60 \times 10^{-19}$ C is the fundamental charge, $k_B = 1.38 \times 10^{-23}$ J K^{-1} is the Boltzmann constant, T is the temperature in K, z_i is the valence and C_i^{∞} is the concentration in ions m^{-3} of the species i. C_i^{∞} can be converted in mol L^{-1} using $C_i^{\infty} = 10^3 n_A C_i^{\infty,m}$ where $C_i^{\infty,m}$ is the concentration in mol L^{-1} and where n_A is the Avogadro's number. Let us denote χ the distance to the surface. There is a linearized solution of this equation, demonstrated in the appendix of Pride (1994) and commonly known as the Debye–Hückel approximation, which allows to express the potential as a function of χ:

$$\psi = \zeta \exp\left(-\frac{\chi}{d}\right). \tag{2}$$

ζ is the potential of the plane that separates the Stern layer from the moving fluid. It cannot be measured directly and always results from a calculation. It is generally negative for quartz at pH>3.

d is a characteristic lengthscale termed as the Debye length, which allows to measure the thickness of the diffuse layer. It is about 10^{-8}–10^{-10} m and depends upon the electrolyte concentration according to

$$\frac{1}{d^2} = \sum_i^n \frac{(ez_i)^2 C_i^\infty}{\varepsilon_0 \varepsilon_r k_B T}. \tag{3}$$

The condition of validity of eq. (2) is that $|\psi| \ll |\frac{k_B T}{e}|$, which corresponds to $|\psi| < 25$ mV at 25 °C.

When the electrolyte flows through the rock, the streaming current created by the displacement of the charges is counterbalanced by a conduction current. The electrokinetic (EK) coefficient is the ratio of the macroscopic potential difference δV created by the conduction current on the pressure difference δP that allows to generate the flow

$$C_S = \frac{\delta V}{\delta P}. \tag{4}$$

The EK coefficient can be expressed as a function of the conductivity of the electrolyte σ_f according to the Helmholtz–Smoluchowski (HS) equation (Overbeek 1952; Hunter 1981):

$$C_S = \frac{\varepsilon_0 \varepsilon_r \zeta}{\eta \sigma_f} \tag{5}$$

where η is the dynamic viscosity of the electrolyte. This equation is derived by considering a single-phase, laminar, monovalent flow in a capillary channel. The demonstration does not consider any surface conductivity effect. It relies on the use of the Debye–Hückel approximation and on the assumption that the thickness of the diffuse layer is small compared to the diameter of the channel ($d \ll R$).

The HS equation provides a consistent prediction of the experimental EK measurements in the standard range of conductivity, from 10^{-3} S m^{-1} up to 10 S m^{-1}. However, the EK coefficient shows deviations at extreme low and extreme high salinities that are not thoroughly understood. The compilation on sands and sandstones used for this study is shown in Fig. 1. Data on glass beads are not reported so as to compare measurements reflecting the same interactions between water and natural quartz.

At high salinity, the EK measurements performed by Jaafar *et al.* (2009) and Vinogradov *et al.* (2010) decrease with increasing concentration, but are still measurable, which is not captured by the classical models of EDL. The conclusion of their work is that considering the salinity dependence of ε_r and η, the ζ potential could be constant or slightly increasing approaching the brine salinity limit. However, the use of the classical variations of ε_r and η in the calculation of ζ are debated (Glover & Déry 2010; Glover *et al.* 2012). There is evidence that the dielectric constant diminishes as one gets closer to the mineral. Such local reduction of the permittivity could yield larger values of ζ potential with increasing salinity.

The measurements at very low salinity (data set 9) are presented in this article. The literature reports few EK coefficient measurements in this extreme low range of salinity, and these measurements are generally presented as a function of the concentration of the initial electrolyte. However, it is observed (Jouniaux *et al.* 2000; Guichet *et al.* 2006; Walker *et al.* 2014) that the conductivity of the electrolyte increases compared to its initial value, if the fluid is left a sufficiently long time to be in equilibrium with the rock. This conductivity increase is the signal of the release of chemical species. Consequently, the concentration that is used for the preparation of the initial electrolyte is not representative of the fluid content at the moment of the measurement, and the EK coefficients plotted versus

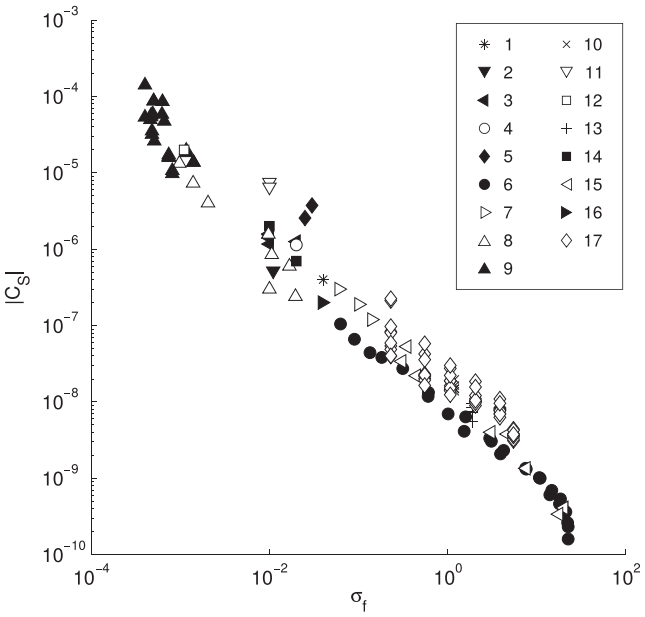

Figure 1. EK coefficient (V Pa^{-1}) as a function of electrolyte conductivity (S m^{-1}) from several studies on sands and sandstones with $5 < \text{pH} < 8$. Data from (1) Ahmad (1964) (sand), (2) Glover *et al.* (2012) (sand), (3) Guichet *et al.* (2003) (sand), (4) Guichet *et al.* (2006) (sand, 98 per cent quartz 2 per cent calcite), (5) Ishido & Mizutani (1981) (quartz grains), (6) Jaafar *et al.* (2009) (sandstone), (7) Jouniaux (sand, personal data), (8) Jouniaux & Pozzi (1997) (sandstone), (9) Jouniaux & Zamora (sandstone, this paper), (10) Li *et al.* (1995) (sandstone), (11) Lorne *et al.* (1999a) (crushed sandstone), (12) Ogilvy *et al.* (1969) (sand), (13) Pengra *et al.* (1999) (sandstone), (14) Perrier & Froidefond (2003) (sandstone), (15) Vinogradov *et al.* (2010) (figures 3, 5 and 8, sandstone), (16) Walker *et al.* (2014) (sandstone), (17) Wang *et al.* (2015) (sandstone).

this concentration can lead, in this domain, to an artificial horizontal plateau. The measurements of the current study are plotted as function of the conductivity and tend to show a vertical increase instead.

The purpose of this article is to model the streaming potential phenomenon using the Lattice Boltzmann (LB) method with a view to understanding these deviations. Similar resolutions of a convection problem coupled to a convecto-diffusive problem using two independent LB equations have been done for other types of electrokinetic and thermal issues (Guo *et al.* 2002; Wang & Kang 2010; Neuville *et al.* 2013; Obliger *et al.* 2013). In this paper, the velocity field and the potential field are simulated in a two dimensional capillary channel using the LB Poisson-Boltzmann solver developed by Chai & Shi (2008). For this study, the advantage of the LB method over the classical analytical resolutions is that it does not require the use of the Debye–Hückel approximation. Furthermore, it puts within reach the assessment of the local variations of the physical quantities at stake. The algorithm presented in this paper is tested in various situations so as to explore the effect of the different parameters that constitute the HS equation. These parameters are the permittivity, the viscosity, the conductivity of the electrolyte, and the ζ potential.

First, light is shed on the effects of pore fluid permittivity and viscosity. Then, the consequence of the Debye–Hückel approximation is quantified by using ζ values that are far beyond the limit of 25 mV. Above this limit, the potential departs from the linear solution given by eq. (2). This departure is maximum in the margins of the capillary, where the electrokinetic coupling occurs.

Table 1. Samples features: porosity (ϕ), permeability (k) and formation factor measured at high salinity (F).

Sample	ϕ	$k\,(10^{-12}\mathrm{m}^2)$	F
Z09	0.19	2.31	10.8
F2Y	0.18	2.02	12.5
Z17	0.17	2.13	15.5
M16	0.15	0.73	17.7
Z19	0.09	0.10	50
Z16	0.07	0.10	36
Z04	0.07	$3\text{–}6 \times 10^{-4}$	105

The electrolyte conductivity is also modified in this area due to the change of ionic distribution approaching the rock mineral. This local dependence of the conductivity is quantified by deriving a model of bulk fluid conductivity which illustrates the influence of the local charge density on the global pore fluid conductivity. Finally, the impact of the electrolyte constituents is analysed, with a particular attention to the effect of non-monovalent counterions.

2 MEASUREMENTS

2.1 Data acquisition

The EK coefficients at the lowest conductivities (data set 9 in Fig. 1) were deduced from streaming potentials, electrical conductivities, and formation factors measured on seven Fontainebleau sandstones. The characteristics of the samples are summarized in Table 1. Porosity was deduced from the difference of weight between the saturated sample and the dry sample. Formation factor was deduced by measuring the electrical sample resistivity and fluid resistivity at high salinity with an impedancemeter at 1 kHz. Permeability was deduced from the Darcy law by measuring the flow rate for six different pressure gradients ranging from 0.01 to 0.1 MPa.

The samples were first saturated with a solution of NaCl prepared at concentration 10^{-5} mol L^{-1}. The electrical potentials were measured while water was made to flow through the samples using the apparatus described by Guichet *et al.* (2006). The tubing circuit was not closed, so that there was no possible electric current leakage through the water within the tubing. Most of the tubing was plastic and the few metallic parts of the apparatus were grounded. The electrical potential was measured with two silver-chloride electrodes of length 40 mm which were made by electrolysis of a silver rod in salt water of concentration 10^{-1} mol L^{-1}. The electrodes were put in the water circuit near the ends of the sample, but not within the water circulation to avoid the electrical noise due to water movement near the electrodes. The two electrodes were connected by two coaxial cables to a high input impedance voltmeter, allowing accurate measurements of the potential. Streaming potential measurements were performed once equilibrium with the rock was attained: water was made to flow through the sample, then collected, transferred to the upstream reservoir and flowed through the sample again. The same procedure was repeated until the conductivity and pH of the water after flowing through the sample were constant. Once the water conductivity and pH were constant, the streaming potential was measured for various water pressure gradients. The measured $\delta V/\delta P$ are gathered in Table 2. The samples denoted with an asterisk correspond to second measurements that were performed some days after the first ones. The water expelled from the sample was also analysed when it was in sufficient quantity (see Section 4.3).

Table 2. Experimental data: sample, temperature, conductivity of the expelled fluid after equilibrium with the rock in mS m^{-1}, $F\sigma_r$ in mS m^{-1}, pH, measured $\delta V/\delta P$ and corrected EK coefficient in V/10^5 Pa. Samples with an asterisk correspond to a second measurement performed some days after.

Sample	$T(^\circ\mathrm{C})$	σ_f	$F\sigma_r$	pH	$\delta V/\delta P$	C_S^{corr}
Z09	21.2	0.63	0.89	6.70	−6.10	−8.57
Z09	21.2	0.62	0.89	6.70	−4.10	−5.85
Z09	21.5	0.66	0.89	6.60	−3.54	−4.75
F2Y	20	0.49	0.58	6.75	−4.97	−5.92
F2Y	20	0.47	0.58	6.85	−4.60	−5.71
F2Y	20	0.47	0.58	6.85	−4.36	−5.41
Z17	21	0.40	0.94	6.70	−6.00	−14.1
Z17	21	0.50	0.94	6.73	−4.63	−8.68
Z17	21	0.50	0.94	6.70	−4.68	−8.78
M16	21	1.16	0.93	6.90	−2.30	−1.84
M16	21	1.16	0.93	6.90	−2.47	−1.98
M16*	18.2	0.40	0.54	6.50	−3.96	−5.35
M16*	18.6	0.46	0.54	6.50	−4.24	−4.98
Z19	17.8	0.48	0.80	6.60	−2.12	−3.54
Z19	17.8	0.48	0.80	6.60	−1.92	−3.19
Z19	17.8	0.51	0.80	6.60	−1.66	−2.61
Z16	18.5	1.40	1.21	6.30	−1.58	−1.37
Z16	18.5	1.40	1.21	6.30	−1.60	−1.38
Z16*	17.3	0.74	0.85	6.70	−1.38	−1.58
Z16*	17.3	0.74	0.85	6.70	−1.43	−1.63
Z16*	17.3	0.74	0.85	6.70	−1.51	−1.72
Z04	18	0.81	1.84	6.60	−0.47	−1.07
Z04	18	0.81	1.84	6.60	−0.43	−0.98

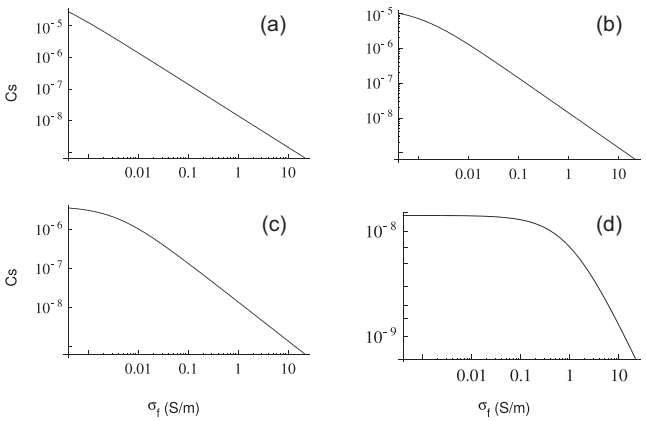

Figure 2. EK coefficient with surface term (eq. 6) as function of fluid conductivity: (a) $2R = 10^{-4}$ m, quartz; (b) $2R = 10^{-5}$ m, quartz; (c) $2R = 10^{-5}$ m, clay; (d) $2R = 10^{-8}$ m, quartz.

2.2 Surface conductivity correction

In this range of salinity, the EK measurements can be impacted by the conductivity of the rock surface (Briggs 1928; Alkafeef & Alajmi 2006; Wang *et al.* 2015). It is possible to quantify the effect of surface conductivity in a capillary channel (Fig. 2) by plotting (Rutgers 1940)

$$C_S = \frac{\varepsilon_0 \varepsilon_r \zeta}{\eta(\sigma_f + \sigma_{\mathrm{surf}})} \tag{6}$$

where $\sigma_{\mathrm{surf}} = \frac{2\Omega}{R}$ (Morgan *et al.* 1989) and where Ω is the conductance of the porous fabric. Depending on the rock composition, this surface conductance can be more or less important, with typical

values of $\Omega = 2.5 \times 10^{-9}$ S for quartz and $\Omega = 8.9 \times 10^{-9}$ S for clay (Revil & Glover 1998). When the surface conductivity is strong (small channel, Fig. 2d), the fluid conductivity becomes negligible in the low salinity domain, and the EK coefficient tends to an horizontal asymptote. For a realistic value of R (above 100 μm) and a surface made of quartz, the EK coefficient seems completely unaffected by the surface conduction (Fig. 2a).

Considering clean Fontainebleau sandstones, composed of more than 99 per cent of quartz (Bourbie & Zinszner 1985), the surface conductivity was measured to be 7–9 $\times 10^{-5}$ S m^{-1} (Ruffet *et al.* 1991). The surface conductivity effect cannot be neglected when the hydraulic radius is of the order of the Debye length, which is encountered below 2×10^{-3} S m^{-1} in that case (Pozzi & Jouniaux 1994). When the rock contains clay, calcite or secondary minerals, the surface conductivity can be stronger, and the limit above which it is negligible can be higher.

In the general case, for realistic rocks, the EK coefficient can be expressed as

$$\frac{\delta V}{\delta P} = \frac{\varepsilon_r \varepsilon_0 \zeta}{\eta F \sigma_r} \tag{7}$$

where F is the formation factor ($\sigma_{\text{fluid}}/\sigma_{\text{rock}}$) measured at high salinity and where σ_r is the rock conductivity measured at the salinity being studied. When the surface conductivity is negligible, $F\sigma_r$ is equal to σ_f and eq. (7) simplifies to the HS equation. The measured $\delta V/\delta P$ ratios of this study are corrected from the surface conductivity using the Overbeek's correction (Overbeek 1952; Jouniaux & Pozzi 1997; Walker *et al.* 2014) defined as

$$C_S^{\text{corr}} = \frac{\delta V}{\delta P}\frac{F}{F_{\text{inst}}} = \frac{\delta V}{\delta P}\frac{F\sigma_r}{\sigma_f}, \tag{8}$$

where F_{inst} is the formation factor at the salinity being studied. The values of σ_r, σ_f and C_S^{corr} are reported in Table 2 with the rest of the data.

3 METHOD

3.1 Numerical process

The numerical process consists in simulating the flow of an electrolyte in a channel on the one hand, the potential created by the accumulation of charges at the fluid-rock interface on the other hand, and coupling these quantities through the computation of the electric field generated by the flow.

Let us denote v the velocity of the electrolyte and ρ_e the electrolyte charge density. By assuming that the conduction current $j_C = \sigma_f E$ counterbalances the streaming current $j_A = \rho_e v$ everywhere, the electric field is expressed locally by

$$\boldsymbol{E}(\chi) = -\frac{\rho_e(\chi) v(\chi)}{\sigma_f}. \tag{9}$$

The local charge density is computed from the species concentrations

$$\rho_e(\chi) = \sum_i^n \rho_i(\chi) = \sum_i^n e z_i C_i(\chi), \tag{10}$$

which obey a Boltzmann distribution

$$C_i(\chi) = C_i^\infty \exp\left(-\frac{z_i e \psi(\chi)}{k_B T}\right). \tag{11}$$

C_i^∞ is the species concentration in the absence of potential field, like when the electrolyte is out of the rock. The concentration in the centre of the pore is similar to C_i^∞, if the condition $d \ll R$ is satisfied.

The conductivity of the electrolyte in the absence of potential field is given by

$$\sigma_f^\infty = \sum_i (e z_i)^2 b_i C_i^\infty, \tag{12}$$

where $b_i = \frac{1}{6\pi\eta R_i}$ is the mobility of the species i, and R_i its effective ionic radius. The computation of eq. (9) using eq. (12) for σ_f is equivalent to assume that the fluid conductivity is similar to the fluid conductivity in the absence of electric field everywhere in the medium, even in the vicinity of the rock surface. This is the approach followed in the derivation of the HS equation. However if we want to consider the actual distribution of the species close to the surface, we should rather compute eq. (9) using

$$\sigma_f^{\text{loc}}(\chi) = \sum_i (e z_i)^2 b_i C_i(\chi), \tag{13}$$

where $C_i(\chi)$ is given by eq. (11). The use of $\sigma_f^{\text{loc}}(\chi)$ allows to consider the excess of positive species that arises approaching the shear plane. This positive excess makes $\sigma_f^{\text{loc}}(\chi)$ vary as a function of the distance to the rock, and consequently impacts the electrical field. In this paper, the conductivity computed from eq. (13) will be termed local conductivity, as opposed to the conductivity from eq. (12), that does not consider the local fluctuations, and which will be termed classical, or standard conductivity.

The simulation process can be summarized in the following steps:

(i) Calculation of the fluid speed norm using an LB algorithm that solves the Navier–Stokes equation.

(ii) Calculation of the electrical potential using another LB algorithm that solves the Poisson-Boltzmann equation: (a) calculation of the electrical potential that depends on the charge density ρ_e; (b) calculation of the concentrations C_i using eq. (11); (c) update of ρ_e using eq. (10).

(iii) Calculation of the electrical field by coupling the fluid speed norm, the charge density and the fluid conductivity according to eq. (9) at each node.

(iv) Calculation of the macroscopic potential difference δV by averaging the field over the whole medium.

(v) Calculation of the EK coefficient defined as $\delta V/\delta P$, δP being the pressure difference that allowed to force the flow.

The parameters ζ and C^∞ are fixed by the user. If the ions of the Stern layer are assumed to be immovable, the Stern layer does not contribute to the coupling in the sense of eq. (9). There is evidence that the Stern layer provides extra-pathways to the current (Werner *et al.* 1998), but this contribution is encapsulated within the surface conductivity effect (Revil & Glover 1998). Considering that the Stern contribution resides in the surface conductivity and that the low-salinity data introduced in this study are corrected from this effect, there is no need to incorporate the Stern layer in this model. The potential that is set at the lateral boundaries is thus considered as equal to ζ (potential of the shear plane). The surface is assumed to be perfectly planar, in accordance to the HS model. Some tests using a realistic rock surface are presented in Appendix.

3.2 LB modelling

The LB method enables to model physical phenomena at fine scale and is well adapted for parallel processing. The fundamental principle of the LB method is the use of numerical fluid particles that

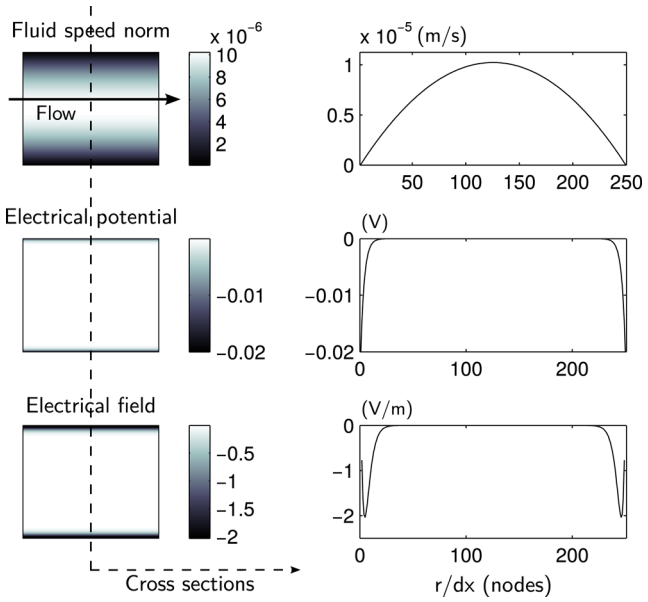

Figure 3. View of the fluid speed norm, electrical potential and electric field in a channel $2R = 10^{-5}$ m, computed with $C^{\infty,m} = 5 \times 10^{-6}$ mol L^{-1} and $\zeta = -20$ mV.

propagate and collide in a fixed number of directions. Let F_i be the probability of presence of a particle in the direction i. In the same direction, let F_i^{eq} be the equilibrium distribution of the particles deriving from entropy and mass conservation principles. The LB equation

$$F_i(\boldsymbol{x} + \boldsymbol{c}_i dt, t + dt) - F_i(\boldsymbol{x}, t) = -\frac{1}{\tau}(F_i - F_i^{\mathrm{eq}}) \tag{14}$$

expresses that at each step for any site x, the change of F_i is proportional to its deviation to the equilibrium distribution. The norms of the velocity vectors in the directions i denoted c_i are given by $c = \frac{dx}{dt}$ where dx and dt are respectively the space and the time steps. The left-hand side of eq. (14) can be interpreted as the displacement of the particles and the right-hand side as the change induced by the collision between the particles. τ is defined as the collision period, giving the collision frequency $\omega = \frac{1}{\tau}$. For convenience, the geometrical configurations of the particle displacements are classified thanks to the acronym DdQq, where d is the dimension of the medium and q is the number of directions available to the particles. A view of the simulations is provided in Fig. 3. The boundary conditions perpendicular to the flow are periodic, which means that everything that flows out of one side, is reinjected by the other side. The borders parallel to the flow are solid, all the particles that reach these frontiers are sent back in the opposite direction.

The full set of equations allowing to reproduce the Navier–Stokes equation is reported in numerous books and articles (Flekkøy 1993; Rothman & Zaleski 1997; Chopard & Droz 1998; Wolf-Gladrow 2005) and will not be reminded here. The geometrical configuration allowing to simulate a classical 2D flow is D2Q9. The time step is given by $dt = dx^2 \frac{\nu^{\mathrm{ad}}}{\nu}$ where ν^{ad} is the adimensional kinematic viscosity of the fluid. ν^{ad} controls the convergence speed of the algorithm through the relationship $\tau = 3\nu^{ad} + 0.5$. For stability reasons, τ must be >0.5, which is achieved with $\nu^{\mathrm{ad}} > 0$. Fig. 4(a) shows the consistency between the simulated fluid speed and the Poiseuille's law given by

$$v(\chi) = \frac{1}{2\eta}\frac{\delta P}{L}(\chi(2R - \chi)), \tag{15}$$

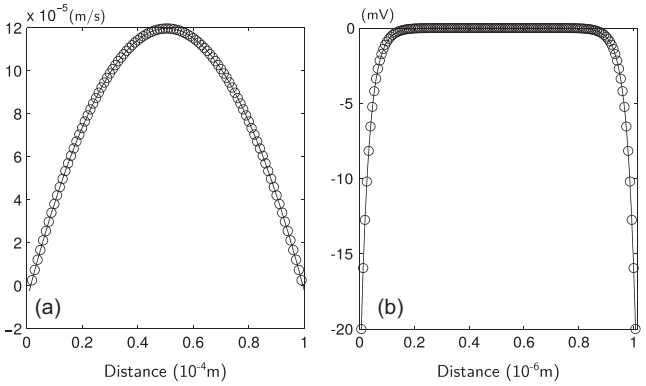

Figure 4. Comparison between the simulations (100 nodes) and the analytical solution (solid line). (a) Simulation of the fluid velocity compared to the Poiseuille's law. (b) Simulation of the electrical potential compared to eq. (2).

where L is the channel length. The precision of the simulated velocity is independent of dx, but is fixed by ν^{ad} and the number of nodes along the velocity profile. With 100 nodes and $\nu^{\mathrm{ad}} < 1$, the relative error on the maximum velocity is less than 0.15 per cent.

The electrical part is simulated with the modified LB model developed by Chai & Shi (2008) in the D2Q5 configuration. Contrary to the previous models that solved a diffusion equation converging to a Poisson equation in stationary regime, this model is a guenine solver of the Poisson–Boltzmann equation, thanks to its modification of the equilibrium distribution function. The correspondance between the simulated potential and eq. (2) appears in Fig. 4(b).

The accuracy of the result compared to the HS equation is controlled by two factors which are the d/dx and $2R/d$ ratios. With the definition that the Debye length is the half of the diffuse layer, the d/dx ratio corresponds to the half of the number of nodes in the diffuse layer. This number controls the precision of the calculation. The $2R/d$ ratio allows to check the validity of the thin double layer assumption invoked in the derivation of the HS equation. The conditions of validity of this assumption are quantified by Jackson & Leinov (2012), who point out that the critical $2R/d$ above which it is acceptable to consider that the thin double layer assumption is verified, is controlled by the surface charge of the capillary. The surface charge depends on the ζ potential and on the ionic strength of the electrolyte. They find that the capillary diameter must be more than 50 times the Debye length for a surface charge <0.2 mC m^2 (low ζ potential, low ionic strength), and more than 400 times the Debye length for a surface charge up to 100 mC m^2 (high ζ value, high ionic strength). Considering that this study focuses on measurements at high salinities and that a wide range of ζ values is to be tested, the lower bound $2R/d = 50$ is not sufficient, but the upper bound $2R/d = 400$ is computationally difficult to reach, and a compromise is to be found.

Let ny be the number of nodes in the direction perpendicular to the rock surface allowing to simulate the potential. By setting ζ at -20 mV and using different values of C^{∞}, R and ny, several EK coefficients are simulated and compared to the HS equation. The corresponding relative error as a function of the d/dx ratio is shown in Fig. 5. For $2R/d = 10$ and $2R/d = 33$, the assumption $d \ll R$ is not verified, which yields a significant relative error. For $2R/d = 104$ and $2R/d = 331$, the relative error decreases with increasing d/dx down to a satisfying value. The number of nodes given by $ny = \frac{2R}{d}\frac{d}{dx}$, must combine a high d/dx with a high $2R/d$ to achieve a good precision. But the use of a high $2R/d$ represents

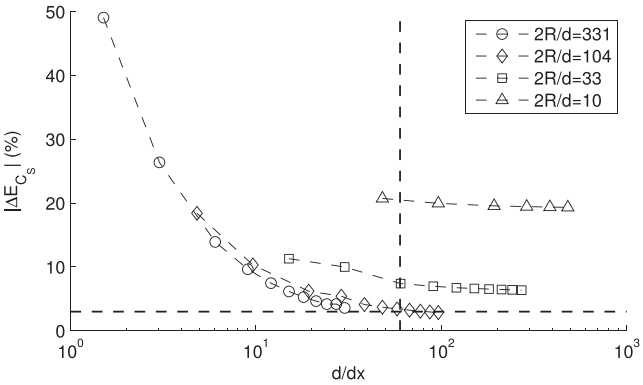

Figure 5. Relative error on C_S versus d/dx for several $2R/d$ ratios. The vertical line is $d/dx = 60$, the horizontal is the limit of 3 per cent.

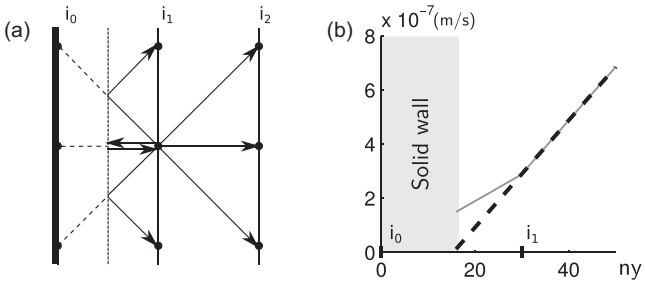

Figure 6. (a) Bounce-back condition on the solid boundary. (b) Interpolation of the fluid velocity.

a heavy computational issue, that makes the power demand hard to manage in the case of large media (see Appendix). By considering that $2R/d = 120$ is sufficiently large to respect the thin double layer assumption, $d/dx = 60$ is found to give a relative error <3 per cent, which is acceptable for the study of the deviations at stake.

Finally, the lower bound of ny is given by $120 \times 60 = 7200$, which is much more than the number of nodes required to simulate the Poiseuille flow. Consequently the flow and the electrical calculation are not performed on the same grid. The coupling of these quantities, which occurs through the computation of the electrical field, requires the 2-D-interpolation of the fluid speed from the hydric mesh to the electrical mesh. This interpolation is made by carefully assessing the position of the zero fluid velocity that is not located at the rock node, due to the bounceback condition. Indeed, the conservation of the distance travelled by the particles in one step makes the zero velocity shift at the middle of the cell (Fig. 6a). Therefore, if the rock wall is located at i_0, and if the first velocity node is located at i_1, the interpolation of the fluid speed between i_0 and i_1 will give an overestimation of the velocity (Fig. 6b, grey line). With $C^{\infty,m} = 0.1$ mol L^{-1} and $\zeta = -20$ mV, the relative error between the simulated EK coefficient and the HS equation is about 7.3 per cent, which is significant, and shows the importance of the first nodes. The calculation of the velocity between the nodes i_0 and i_1 by interpolating the velocity between i_1 and i_2 makes the relative error drop to 2.1 per cent (black dashed line).

For time performance reasons, C_S is calculated every 10 steps. The procedure stops when the EK coefficient is stabilized (relative change between two C_S calculations $<10^{-10}$).

3.3 Validity of the LB approach

Several tests are performed in order to verify that streaming potentials are properly modelled by the LB approach. By running the

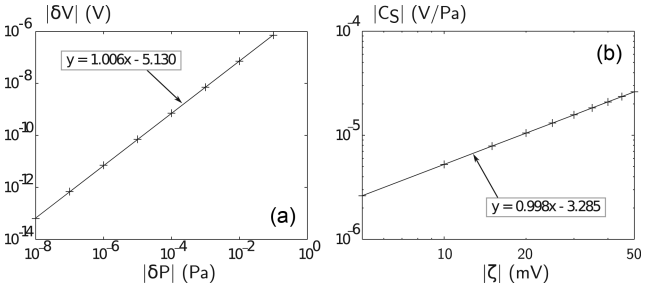

Figure 7. Simulations in channel $2R = 10^{-6}$ m with $C^{\infty,m} = 10^{-4}$ mol L^{-1}. (a) Simulated δV versus imposed δP. (b) EK coefficient versus $|\zeta|$.

simulations for several values of δP the proportionality between δP and the calculated δV is verified (Fig. 7a). Starting from now, all the simulations are done with $\delta P = 10^{-2}$ Pa. The proportionality between the simulated EK coefficient and the imposed ζ is also checked (Fig. 7b). Finally, it is verified that the EK coefficient is independent of the channel length.

The EK coefficient is compared to the analytical solution given by the volumetric average of j:

$$C_S = -\frac{\langle j \rangle}{\sigma}\frac{L}{\delta P} \tag{16}$$

with

$$\langle j \rangle = \frac{1}{\pi R^2 L}\int_0^L \int_0^{2\pi} \int_0^R v(r)\rho_e(r) r \, \mathrm{d}r \, \mathrm{d}\theta \, \mathrm{d}l \tag{17}$$

where r is the distance from the centre of the capillary towards the rock surface. In cylindrical coordinates, the Poiseuille's law reads

$$v = \frac{1}{4\eta}\frac{\delta P}{L}(R^2 - r^2) \tag{18}$$

and the charge density of a NaCl reads

$$\rho_e = -2eC^{\infty} \sinh\left(\frac{e\psi(r)}{k_B T}\right), \tag{19}$$

which gives, using the Debye–Hückel approximation,

$$C_S = \frac{\zeta}{\eta(b_{Na} + b_{Cl})k_B T}\int_0^R r\left(1 - \frac{r^2}{R^2}\right) \mathrm{e}^{-\frac{R-r}{d}} \mathrm{d}r. \tag{20}$$

It is noteworthy that the dependence on the salinity resides only in the parameter d. This equation is plotted as a function of the $2R/d$ ratio and compared to the HS equation and the simulations in Fig. 8. In the high $2R/d$ domain, the 3 approaches are merged together. When $2R/d$ decreases, the diffuse layers of the opposite planes start to overlap (cross-sections B), until the potential has no place enough to collapse to zero (cross-section A). As the thin double layer assumption gets less valid, the calculated EK coefficient diverges from the HS equation. At very low $2R/d$, the EK coefficient clusters on a horizontal plateau. This horizontal plateau is due to the fact that when the opposite planes are very close, the potential has no room to decay from the ζ value, and remains constant everywhere in the channel. In that case, the EK coefficient is given by

$$C_S = \frac{R^2}{4e\eta(b_{Na} + b_{Cl})} \sinh\left(\frac{e\zeta}{k_B T}\right). \tag{21}$$

If the potential happens to be non-zero where the fluid should be neutral, the EK coefficient departs from the HS relationship. For a negative potential, as encountered at low $2R/d$ with a negative ζ value, the EK coefficient is lower. The simulations follow the trend given by the analytical solution, and the LB model is shown

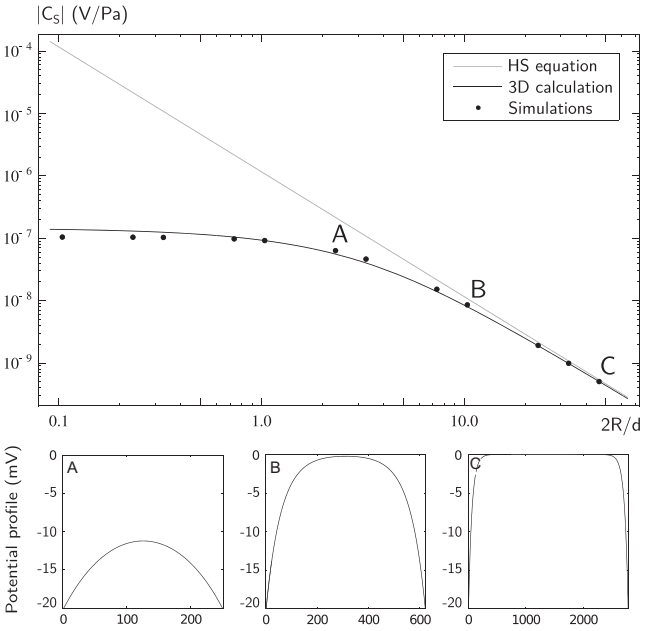

Figure 8. Top: C_S versus $2R/d$ for $\zeta = -20$ mV and $R = 10^{-8}$ m (varying concentration). Helmholtz–Smoluchowski equation in grey, 3-D analytical solution (eq. 20) in black, simulations in dots. Bottom: potential cross-sections for three $2R/d$ values. A: $2R/d \sim 2$; B: $2R/d \sim 10$; C: $2R/d \sim 46$.

to be reliable even in this configuration, sometimes called the thick double layer model.

4 RESULTS

The LB model presented in the previous section is now used to explore the effect of the different parameters constituting the HS equation.

4.1 Salinity dependence of permittivity and viscosity

In standard conditions of temperature, the commonly used values of viscosity and permittivity are constants, independent of the concentration. For high salinities, the use of constants becomes incorrect, and proper models are required.

The dielectric constant of water as function of salinity was given by G.R. Olhoeft (unpublished notes, Revil *et al.* 1999b):

$$\varepsilon_r(T, C) = \varepsilon_r(T) + \sum_{i=1}^{3} c_i C^i, \tag{22}$$

where $c_1 = -13$ L mol^{-1}, $c_2 = 1.065$ (L mol^{-1})^2, $c_3 = -0.03006$ (L mol^{-1})^3 and $\varepsilon_r(T) = 80.1$ at 20 °C. This relationship yields a permittivity that is roughly constant below 0.1 mol L^{-1}, and that drops from 80 to 35 at the brine salinity limit (Fig. 9a). This behaviour is supported by the recent analytical model of Levy *et al.* (2012).

In parallel, the value of the dynamic viscosity increases by a factor 2 above 0.1 mol L^{-1} (Fig. 9b). The viscosity relationship above this limit is derived using the data from (Lide 2005), also used by Vinogradov *et al.* (2010):

$$\eta(C) = \sum_{i=0}^{5} b_i C^i, \tag{23}$$

where $b_0 = 1.0063$, $b_1 = 7.7674 \times 10^{-2}$, $b_2 = 1.0682 \times 10^{-2}$, $b_3 = 2.8167 \times 10^{-3}$, $b_4 = -8.1438 \times 10^{-4}$, $b_5 = 1.1633 \times 10^{-4}$ and where η is in mPa s. Below 0.1 mol L^{-1}, the standard value $\eta = 1.002$ mPa s is kept.

The LB modelling allows to take into account the effect of the dielectric constant through its occurrence in the source therm of the Poisson–Boltzmann equation. The viscosity governs the amount of collisions of the particles controlling the rheology of the fluid, and is involved in the computation of the conductivity.

In this section, the choice is made to present the EK coefficient as a function of the electrolyte concentration because of the conductivity variations observed in the high salinity domain. At medium and low salinities, conductivity and concentration are proportional, following the trend of eq. (12). At high salinity, the conductivity increases less than expected with increasing concentration (Fig. 9c). This compels to present the EK measurements as a function of the concentration, to avoid any artificial deviation due to the conductivity behaviour. Two reciprocal conductivity-concentration relationships valid over the whole range of salinity are derived by combining the high salinity measurements (Jaafar *et al.* 2009, personal communication) at concentration above 5×10^{-3} mol L^{-1}, to eq. (12) below 5×10^{-3} mol L^{-1} (Fig. 9d):

$$\log \sigma_f^{\infty} = \sum_{i=0}^{5} a_{1i} (\log C^{\infty,m})^i \tag{24}$$

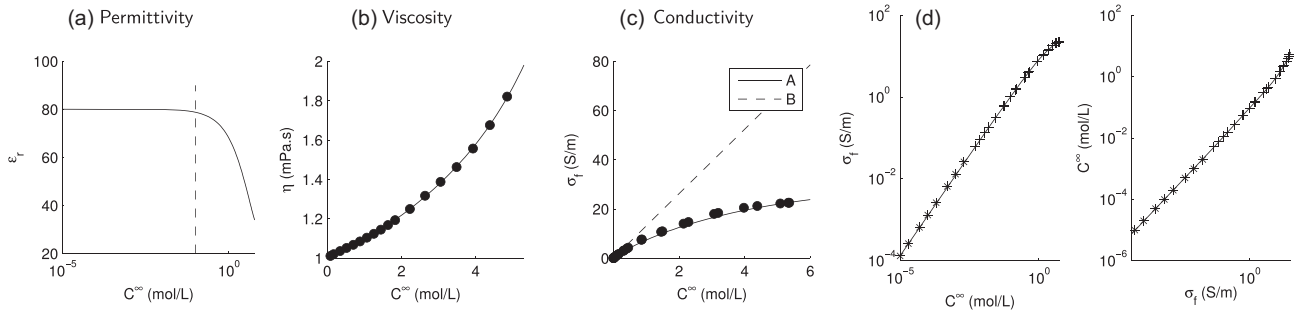

Figure 9. (a) Dielectric constant of water versus concentration (G.R. Olhoeft; (Revil *et al.* 1999b)). The vertical dashed line corresponds to the 0.1 mol L^{-1} limit. (b) Viscosity versus concentration (eq. 23, data from Lide 2005) (c) Conductivity versus electrolyte concentration (data from Jaafar *et al.* 2009). A: corrected Sen & Goode (1992) empirical equation; B: eq. (12). (d) Conductivity–concentration relationships (eqs 24 and 25) derived from the experimental data of Jaafar *et al.* (2009) ('+' symbols, $C^{\infty,m} > 5 \times 10^{-3}$ mol L^{-1}), and data calculated from eq. (12) ('*' symbols, $C^{\infty,m} < 5 \times 10^{-3}$ mol L^{-1}).

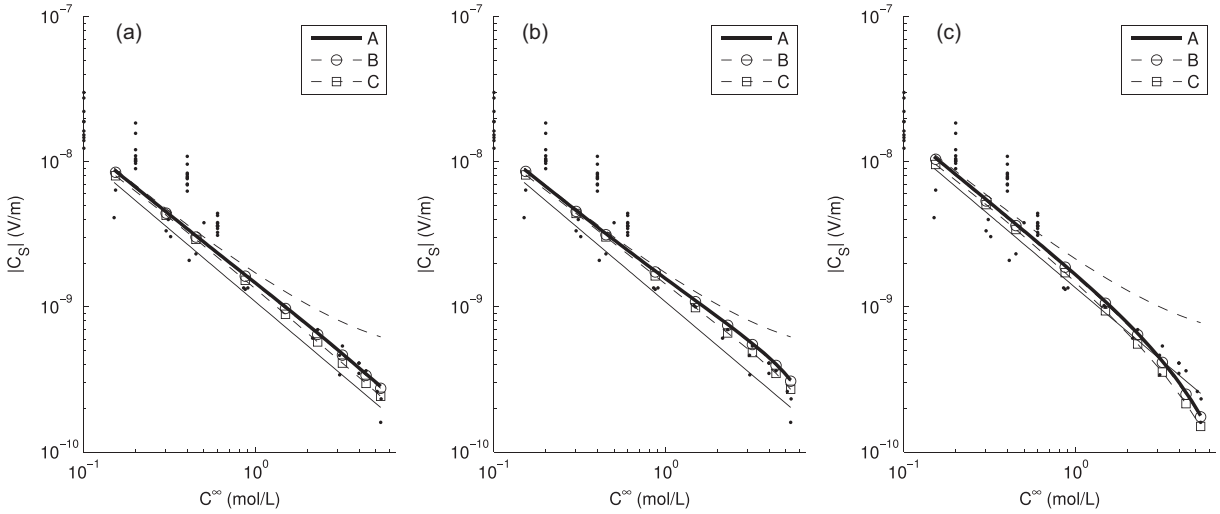

Figure 10. EK coefficient in the high-salinity domain. Data in black dots: Jaafar *et al.* (2009); Vinogradov *et al.* (2010); Wang *et al.* (2015). The thin solid line is the HS equation, computed with eq. (12) and constant permittivity and viscosity (reference). The dashed line is the HS equation computed with eq. (24) and constant permittivity and viscosity. A, B and C are respectively the HS equation, the simulations with the classical conductivity and the simulations with a local conductivity computed with eq. (24) and: (a) a constant viscosity and the permittivity from eq. (22) ($\zeta = -20$ mV); (b) a constant permittivity and the viscosity from eq. (23) ($\zeta = -20$ mV); (c) by using both of the permittivity and viscosity variations given by eqs (22) and (23) ($\zeta = -25$ mV).

with $a_{15} = -0.0013273$, $a_{14} = -0.01717$, $a_{13} = -0.0801$, $a_{12} = -0.17312$, $a_{11} = 0.77962$ and $a_{10} = 0.91778$,

$$\log C^{\infty,m} = \sum_{i=0}^{7} a_{2i} (\log \sigma_f^\infty)^i \tag{25}$$

with $a_{27} = 5.4958 \times 10^{-4}$, $a_{26} = 6.1177 \times 10^{-3}$, $a_{25} = 0.02464$, $a_{24} = 0.040537$, $a_{23} = 0.014129$, $a_{22} = -0.011477$, $a_{21} = 1.0552$ and $a_{20} = -1.0246$.

The impact of the permittivity and viscosity variations on the EK coefficient in the high salinity domain is quantified in Fig. 10, by comparing the HS equation (A, thick line), the simulations with the classical conductivity (B, circles) and the simulations with the local conductivity (C, squares), all computed using eq. (24), to the experimental data (dots). The thin solid line corresponds to the HS equation, computed with the conductivity of eq. (12) and constant viscosity and permittivity. It stands for reference for comparison to the deviations observed experimentally. The dashed line is the HS equation, computed with the conductivity from eq. (24). It shows an upward curvature that is the result of this less increasing conductivity approaching the brine salinity limit. The simulations with the local conductivity are performed by adapting the species mobilities such as $b_{Na} = B/(1 + R_{Na}/R_{Cl})$ and $b_{Cl} = B/(1 + R_{Cl}/R_{Na})$, with $B = \sigma_f^\infty/(10^3 n_A e^2 C^{\infty,m})$.

In all cases, we can observe a good consistency between the three approaches. Fig. 10(a) shows A, B and C computed using a constant viscosity and a salinity-dependent permittivity. The permittivity decrease with increasing salinity counteracts the EK coefficient increase that results from the conductivity increasing less with salinity in the high salinity domain. Fig. 10(b), shows that the salinity dependence of viscosity counteracts the effect of conductivity in a similar way. However, the combination of both effects is required to make the EK coefficient pass under the reference and drop at the extreme high salinities (Fig. 10c). It is noteworthy that the three curves fit the experimental data with a constant ζ potential of about -25 mV. The competition between the viscosity, permittivity and conductivity fluctuations allows to account for the EK coefficient deviation at high salinity, without the need of an additional ζ variation. This observation corresponds to the findings of Jaafar *et al.* (2009); Vinogradov *et al.* (2010), who calculated the ζ values corresponding to their measurements taking into account the salinity dependence of ε_r and η, and obtained a constant or slightly increasing trend in the high salinity domain.

However, the question of the proper choice of the viscosity and the permittivity, points out that these quantities may fluctuate within the EDL as one gets closer to the mineral (Grahame 1947). Such decrease of permittivity and viscosity in the vicinity of the mineral could yield an increasing ζ with increasing salinity, instead of a constant ζ (Glover & Déry 2010; Glover *et al.* 2012). A model of local dielectric constant was derived by Booth (1951); Hunter (1966)

$$\varepsilon_r(T, C, \chi) = \varepsilon_r(T, C) \left[1 - \beta \left(\frac{\mathrm{d}\psi(\chi)}{\mathrm{d}\chi} \right)^2 \right] \tag{26}$$

with $\beta = 4 \times 10^{-18}$ m^2 V^{-2} for water at 25 °C. Pride & Morgan (1991) showed that this variation can be safely neglected for salinities <0.1 mol L^{-1}. At high concentration, the term containing the potential derivative becomes important due to the sharp decrease of the potential in the diffuse layer. By assuming that ζ is sufficiently low in this range of salinity to apply the Debye–Hückel approximation, eq. (26) becomes

$$\varepsilon_r(T, C, \chi) = \varepsilon_r(T, C) \left[1 - \beta \left(\frac{\psi(\chi)}{d} \right)^2 \right]. \tag{27}$$

With $\zeta = -25$ mV and $C^{\infty,m} = 5.33$ mol L^{-1} (maximum salinity of the data set), the dielectric constant drops from 35.6 to 29.2 at the margins of the capillary. By injecting this relationship in the algorithm and using the classical conductivity, the simulated EK coefficient amounts to 1.69×10^{-10} V Pa^{-1}, versus 1.78×10^{-10} V Pa^{-1} with a non-local ε_r. This difference is of the order of magnitude of the simulations precision, which is observable, but small. Using this model, the effect of the local variations of ε_r appears too weak to impact the derivation of ζ potentials. The result is similar with a local conductivity.

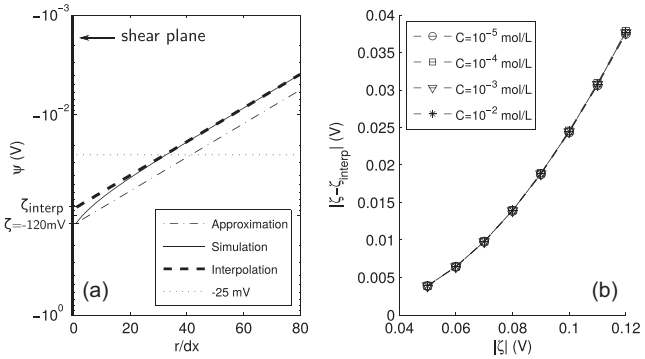

Figure 11. (a) Zoom on the potential near the walls. The analytical solution (approximation) is eq. (2). (b) Difference between ζ and ζ_{interp} for several concentrations as a function of ζ.

It is not possible to simulate the local variations of fluid viscosity with this algorithm, because it would compel to use a space dependent collision period, which would breach the momentum conservation on which the LB method is based. However, the local viscosity model given by Booth (1951); Hunter (1966) is of the same type of eq. (26), and it can be assumed that the local viscoelectric effects can be neglected in a similar way.

The following sections will exclusively focus on the deviation observed at low salinity. Considering that permittivity and viscosity vary with the concentration in a salinity range that is far away from this domain, they will be kept constant starting from now.

4.2 Local variations of pore fluid conductivity

After the permittivity and the viscosity, another key parameter constituting the HS equation is the ζ potential. The HS equation relies on the Debye–Hückel approximation, which is valid only if the potential remains below 25 mV. Considering that the most commonly used models of ζ potential generate values that are far above this limit (Kirby & Hasselbrink 2004), it is interesting to quantify the error introduced by this approximation. In particular, this section aims at determining if this error is concentration-dependent, and how this impacts the bulk fluid conductivity. Strong ζ values up to -130 mV are introduced in the LB model, with a view to detecting deviations of C_S with decreasing salinity.

4.2.1 Estimation of the error induced by the Debye–Hückel approximation

The Debye–Hückel approximation expresses that the potential decays from the shear plane following the trend given by eq. (2), which is linear in semi-log scale. When the potential of the shear plane is high, this approximation is not valid anymore, and the trend that is actually followed by the potential departs from this linearity. Such departure can be observed in Fig. 11(a) where the potential simulated in a channel (solid line) is compared to the potential given by eq. (2). Starting from the shear plane where the potential is set to -120 mV, we can observe the formation of a gap between the simulations and the analytical solutions that increases until the potential achieves -25 mV. After -25 mV, the simulated potential follows the same linear trend as eq. (2), and the gap resulting from the first part of the decrease remains constant. It is possible to measure the importance of this gap by interpolating a 'true' ζ potential using the linear part of the simulated potential, where $|\psi| < 25$ mV (thick dashed line).

The difference between ζ and ζ_{interp} is computed for several ζ and several concentrations. As it could be expected, Fig. 11(b) reports that the higher ζ, the higher the difference, since the approximation becomes less valid with increasing ζ. The Debye–Hückel approximation is valid in the centre of the medium, where the potential is zero, but it gets less precise closer to the surface, and this effect is more pronounced when the ζ value is strong compared to $\frac{k_B T}{e}$. For $\zeta = -120$ mV, the difference amounts to 40 mV. For high surface charges, the potential experienced by the ions is less important that the one given by the approximation. However, the curves computed for several C^∞ show an exact superposition, meaning that this difference is independent of the concentration.

The use of high ζ values triggers a non-linearity of the potential in the vicinity of the shear plane. This non-linearity increases with increasing ζ, but is independent of C^∞. This non-linearity fades out as soon as the limit of 25 mV is reached, which is achieved at a short distance from the shear plane. The question to be solved now is, to what extent this deviation is able to impact the fluid conductivity, and then the streaming current.

4.2.2 Impact on the species distribution

The potential non-linearity is independent of the concentration. However, the potential governs the distribution of the species in the capillary according to eq. (11). The ionic distribution is required to calculate the charge density, but also the electrolyte conductivity. In other words, the electrolyte conductivity is likely to be influenced by the potential non-linearity through the impact of the potential on the species distribution. In this section, simulations with a local conductivity are compared to simulations with the classical conductivity in order to assess if ζ impacts significantly the bulk fluid conductivity, and again, if this impact is concentration dependent.

The tests are performed with $\zeta = -20$ mV and $\zeta = -80$ mV in two situations: R is fixed, or R is adapted so as to keep $2R/d = 120$. When R is fixed, the $2R/d$ ratio decreases with decreasing concentration. The small $2R/d$ situation is interesting because in that case, the non-linear part of the potential represents a significant portion of the potential profile. A radius $R = 10^{-6}$ m allows to test this configuration, without having a complete overlapping of the diffuse layers. The case where $2R/d$ is fixed at a large value allows to avoid the geometrical deviation of C_S with decreasing concentration (see Section 3.3) and then, to assess the impact of ζ alone.

In Fig. 12, the solid symbols are the EK coefficients simulated with the standard conductivity, whereas the open symbols represent the simulations with a local conductivity. The case $\zeta = -80$ mV is in grey, the case $\zeta = -20$ mV is in black. The simulations with a constant R are in dotted lines, the simulations with a fixed $2R/d$ are in dashed lines.

In the case of the fixed $2R/d$ ratio, when the conductivity is not local dependent, the simulations are more or less merged with the HS equation, even for the high ζ value. This means that the potential non-linearity highlighted in the previous section has a weak impact on the computation of the charge density. On the contrary, when the simulations are realized with a local conductivity, the simulated EK coefficient is lower than the HS equation. The difference is more important at a high ζ value, and, again, independent of the concentration.

The same kind of gap can be observed with the simulations using a constant radius, unless in the very low salinity domain, where the diffuse layers start to overlap. At low $2R/d$, the EK coefficient

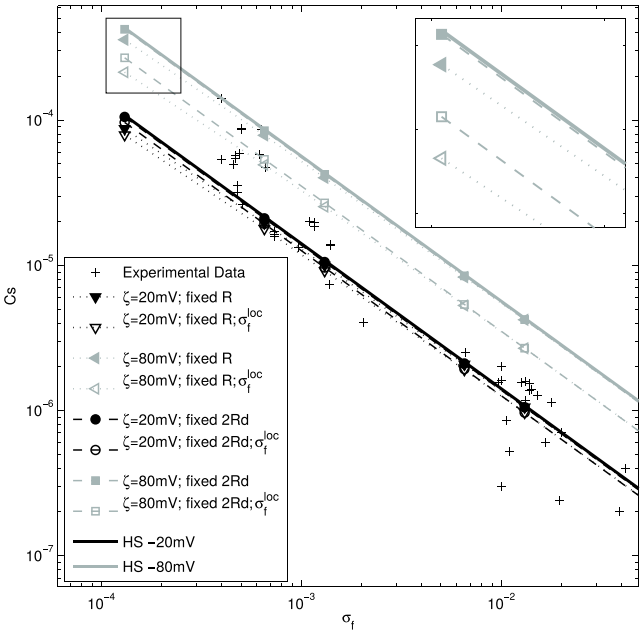

Figure 12. Comparison of the C_S values calculated with the standard σ_f^∞ (solid symbols) and the local σ_f^{loc} (open symbols). For both $\zeta = -20$ mV and $\zeta = -80$ mV, C_S varies in a channel of fixed R, or with R that changes so as to follow the variation of the Debye length (fixed $2R/d$). The HS equation is drawn in solid line.

initiates the downward curvature that was reported in section 3.3, but not the expected upward deviation.

In summary, the species distribution in the vicinity of the mineral has a great impact on the EK coefficient through the bulk fluid conductivity. The change of distribution approaching the mineral stems from the potential. The linear approximation of the potential, used in the HS equation, was found to yield significant discrepancies in the previous section. But the effect of these discrepancies on the charge density and bulk fluid conductivity remains independent of C^∞.

4.2.3 Computation of a bulk fluid conductivity model

A convenient way to quantify the bulk fluid conductivity, that will be denoted σ_f^*, is to express it as the conductivity that must be injected in the HS equation to obtain the same EK coefficients as the simulated values. By definition,

$$\sigma_f^* = \frac{C_S^\infty}{C_S^{\text{sim}}}\sigma_f^\infty, \tag{28}$$

where σ_f^∞ is the classical conductivity calculated with eq. (12), C_S^∞ is the EK coefficient calculated with eq. (5) using σ_f^∞, and C_S^{sim} is the EK coefficient simulated with a local conductivity.

Fig. 13(a) shows the σ_f^* obtained with several concentrations and several ζ in semi-log scale. Fig. 13(b) shows the same σ_f^* divided by the concentration that was used for their computation. This highlights that the σ_f^*/C^∞ ratios are the same for the three concentrations. It can be inferred from this that the bulk fluid conductivity is proportional to the concentration of the electrolyte injected in the sample, and that it is a polynomial function of the ζ potential:

$$\sigma_f^*(\zeta, C^{\infty,m}) = C^{\infty,m}(a_3\zeta^3 + a_2\zeta^2 + a_1\zeta + a_0) \tag{29}$$

with $C^{\infty,m}$ in mol L^{-1}, ζ in V, $a_3 = 1511.5$, $a_2 = 689.15$, $a_1 = -50.354$ and $a_0 = 13.346$.

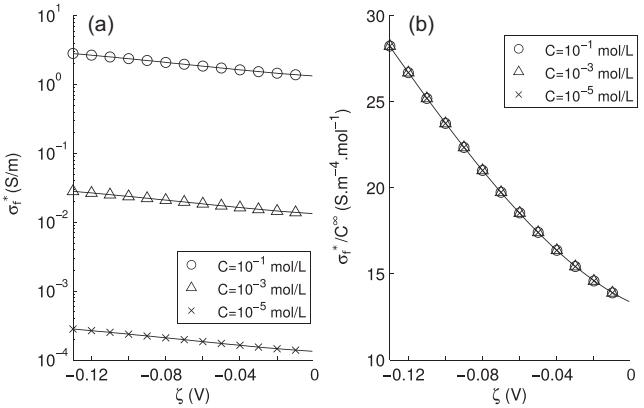

Figure 13. Bulk fluid conductivity deduced from the simulations. (a) Bulk fluid conductivity as a function of ζ for three different concentrations in semi-log scale. (b) Bulk fluid conductivity divided by C^∞ as a function of ζ. Eq. (29) in solid line.

It is noteworthy that when ζ tends to zero, σ_f^* tends to the conductivity measured out of the rock, which is similar to the local conductivity at the centre of the pore, if $d \ll R$.

An analytical expression of the bulk fluid conductivity can be derived by calculating the EK coefficient through the integration of the electrical field over the whole space:

$$\langle E \rangle = \frac{1}{\pi R^2 L}\int_0^L\int_0^{2\pi}\int_0^R \frac{v(r)\rho_e(r)}{\sigma_f^{\text{loc}}(r)} r\,\mathrm{d}r\,\mathrm{d}\theta\,\mathrm{d}l. \tag{30}$$

The fluid velocity is given by the Poiseuille's law, the charge density by eq. (10), the fluid conductivity by eq. (13). Using the Debye–Hückel approximation,

$$\langle E \rangle = -\frac{\delta V}{L} = -\frac{\delta P}{L}\mathcal{I} \tag{31}$$

where

$$\mathcal{I} = \int_0^R -\frac{r(R^2-r^2)\sum_i z_i e C_i^\infty\left(1-\frac{z_i e\zeta}{k_B T}\mathrm{e}^{-\frac{(R-r)}{d}}\right)}{2\eta R^2\sum_i (z_i e)^2 b_i C_i^\infty\left(1-\frac{z_i e\zeta}{k_B T}\mathrm{e}^{-\frac{(R-r)}{d}}\right)}\mathrm{d}r \tag{32}$$

is the resulting EK coefficient. The equalization of eq. (32) to the HS equation expressed with σ_f^* leads to

$$\sigma_f^* = \frac{\varepsilon_0\varepsilon_r\zeta}{\eta\mathcal{I}}. \tag{33}$$

This solution is valid whatever the nature of the ionic species, monovalent or polyvalent, and will be used later in this study. For a 1:1 electrolyte such as NaCl, eq. (32) simplifies to

$$\mathcal{I} = \int_0^R \frac{r(R^2-r^2)Ae^{-\frac{(R-r)}{d}}}{\eta R^2(e(b_{\text{Na}}+b_{\text{Cl}}) - e(b_{\text{Na}}-b_{\text{Cl}})Ae^{-\frac{(R-r)}{d}})}\mathrm{d}r \tag{34}$$

with $A = \frac{e\zeta}{k_B T}$. This expression is compared to the simulations realized at $C^{\infty,m} = 0.1$ mol L^{-1} in Fig. 14(a). The comparison is expected to be similar whatever the value of C^∞, since the effect of the local conductivity was shown to be independent of C^∞ in the previous section. The fact that eqs (32) and (34) were derived using the Debye–Hückel approximation allows to decipher whether the impact of the local conductivity fully derives from the better consideration of the ionic distribution at the fluid-rock interface, or if the non-linearity of the potential also contributes to this effect. Both approaches agree for the lowest ζ values, but the discrepancy rapidly increases as ζ increases. This discrepancy between the σ_f^*

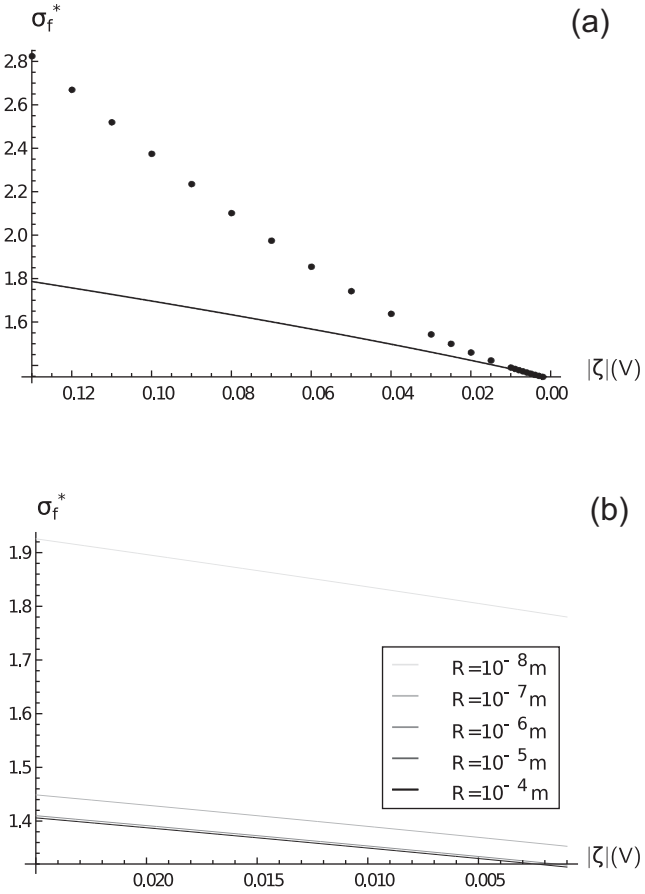

Figure 14. (a) Comparison between σ_f^* computed from the simulations (dots) (see also eq. 29) and σ_f^* computed from eq. (33) (solid line) with $C^{\infty,m} = 0.1$ mol L^{-1} and $R = 1.16 \times 10^{-7}$ m. (b) Effective conductivity calculated from eq. (33) for $C = 0.1$ mol L^{-1} and several R.

computed from eq. (29) (simulations) and the σ_f^* computed from eq. (33) is evidence that the Debye–Hückel approximation introduces a significant error. Their ratio amounts to 1.5 for the strongest tested ζ.

An important parameter that must be analysed for the validity of these relationships is the sensitivity of σ_f^* to the channel size. σ_f^* is computed for several R at $C^{\infty,m} = 0.1$ mol L^{-1} (Fig. 14b). Again, the results are expected to be the same whatever the value of C^∞, provided C^∞ is sufficiently low to be in the range where ε_r and η are constant. We can observe that the bulk fluid conductivity converges to a value that is determined by ζ and C^∞ with increasing R. If R is too small, σ_f^* is influenced by the diffuse layers overlapping. Above a sufficiently large R, the portion of non-zero potential remains constant, and all increments of capillary diameter merely widen of the portion of channel that does not contribute to the coupling. This results in a convergence toward a bulk fluid conductivity that is independent of the size of the medium. We can notice that this stabilization occurs for a value of R that is rather low (discrepancy <0.3 per cent when $R > 10^{-6}$ m for this concentration), which is a good point for the applicability of this relationship.

In this part, an expression of the bulk fluid conductivity was derived numerically and analytically. This conductivity illustrates a better consideration of the ionic distribution at the fluid-rock interface. The excess of positive species induces a conductivity enhancement which depends on ζ, on the nature of the species, but not on the salinity. The numerical expression provides an insight on the error introduced by the Debye–Hückel approximation, whereas the analytical form is valid for any type of electrolyte, and will be used in the following section.

Table 3. Chemical analysis of the water after circulating within the samples tested at low salinities. Compositions in mg L^{-1}, charge density in C m^{-3}. The sample marked by an asterisk corresponds to a second measurement. ρ_e^∞ is the calculated charge density.

Sample	Na	K	Ca	Mg	Cl	SiO_2	ρ_e^∞
F2Y	0.44	0.36	0.8	0.06	0.43	0.26	4109
M16	1.92	0.7	0.46	0.09	1.45	0.3	5307
M16*	0.26	0.12	0.34	0.02	0.3	0.17	1772
Z09	0.44	0.2	0.6	0.04	0.4	0.21	3465
Z16	0.45	0.3	0.64	0.05	0.5	0.34	3261
Z17	0.42	0.14	0.38	0.03	5.8	0.21	−12264
Z19	0.31	0.12	0.54	0.03	0.3	0.21	3022

4.3 Chemical effects at low salinities

It was pointed out in the introduction, that the conductivity undergoes a long time to equilibrate with the sample when the measurements are performed in the low salinity domain. In the current study, the measurements were made with a solution of NaCl initially prepared at 10^{-5} mol L^{-1}. After flowing through the sample and being in equilibrium with the rock, an increase of this conductivity was observed. Such increase is the signature of a chemical event. It can be reasonably assumed that the pure initial water attacked the rock and dissolved some particles which joined the electrolyte. Table 3 shows the main components that were measured in the solutions after the measurements. These analyses show the presence of Ca^{2+} and Mg^{2+} ions that indicate the presence of calcite in the initial rock. It can be argued that these species would also have been measured with an initial water slightly more concentrated, but probably in a lower proportion (the more concentrated, the less aggressive the water), and would have been overwhelmed by the presence of Na^+ and Cl^-. This section aims at understanding the impact of such modification of the fluid composition.

4.3.1 Non-monovalent species

Considering the presence of non-monovalent species, this study starts by assessing the impact of the species valences on the EK coefficient. Two EK coefficients are simulated with a NaCl electrolyte and a $CaCl_2$ electrolyte with a conductivity $\sigma_f^\infty = 4.34 \times 10^{-4}$ S m^{-1}. This conductivity is achieved with a concentration $C^{\infty,m} = 3.31 \times 10^{-5}$ mol L^{-1} for NaCl and $C^{\infty,m} = 10^{-5}$ mol L^{-1} for $CaCl_2$, with the assumption that $C_{Cl}^\infty = 2C_{Ca}^\infty$.

The HS equation does not make the difference between the two kinds of electrolyte, and gives the value -3.26×10^{-5} V Pa^{-1} for both of them. The EK coefficients computed from eq. (32) give -3.00×10^{-5} V Pa^{-1} for NaCl and -2.33×10^{-5} V Pa^{-1} for $CaCl_2$. The EK coefficients simulated with a local conductivity are -2.93×10^{-5} V Pa^{-1} for NaCl and -2.40×10^{-5} V Pa^{-1} for $CaCl_2$. It can be reminded that the analytical derivation of the EK coefficient with the bulk fluid conductivity allows to comprehend the distribution of the species at the fluid-rock interface, while the simulations with the local conductivity enable, in addition, to avoid the use of the Debye–Hückel approximation.

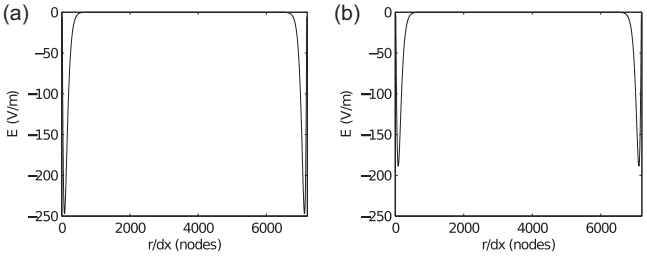

Figure 15. Electrical field simulated with $\zeta = -20$ mV. (a) NaCl $C^{\infty,m} = 3.31 \times 10^{-5}$ mol L^{-1}. (b) CaCl2 $C^{\infty,m} = 10^{-5}$ mol L^{-1}.

In both cases, the EK coefficients computed with the valences of $CaCl_2$ are inferior to the EK coefficients computed with the valences of NaCl. For the coefficients derived analytically, the ratio between NaCl and $CaCl_2$ amounts to 1.28, while it amounts to 1.22 for the simulated coefficients. This means that to reach the EK coefficient obtained with NaCl, the ζ potential of $CaCl_2$ must be multiplied by approximately 1.25, giving -25 mV, instead of -20 mV. When the calculation is made with $\zeta = -80$ mV, this ratio amounts to 1.43, which requires $\zeta = -115$ mV instead of -80 mV for $CaCl_2$.

As a rule, the valence of the negative ion is of negligible importance, since the decrease of the amount of negative species approaching the mineral is approximately the same whatever ζ. On the contrary, the amount of positive species varies a lot with ζ, which enhances the sensitivity to the positive valence. According to eq. (32) the contribution of the valence appears mainly through the conductivity, due to the $(ez_i)^2$ term. Using a non-monovalent counterion, the charge density and the local conductivity both increase compared to NaCl, but the increase of the conductivity overcomes the increase of the charge density, and results in a lower electrical field, as shown by Fig. 15. This lower electrical field yields a lower potential difference, and then a lower EK coefficient.

The consequence of these results is that deriving ζ potentials of polyvalent species using the HS equation introduces a significant error. This error stems from the lack of consideration of the fluid conductivity enhancement near the interface, that lowers the EK coefficient. This decrease of EK coefficient is generally interpreted as a decrease of ζ potential with increasing valence. We can observe here that the ionic valence decreases the EK coefficient mechanically, even in the absence of ζ variation.

4.3.2 Species release in the low salinity domain

The fluids expelled from the samples were analysed whenever possible. The main chemical components present in the solutions are listed in Table 3. The total charge density is computed by combining eqs (10) and (11), which gives

$$\rho_e^{\infty} = \sum_i^n \rho_i^{\infty} = \sum_i^n e z_i C_i^{\infty}. \tag{35}$$

The charge densities computed from the chemical analyses are systematically non-zero due to the fact that these analyses are not exhaustive. We assume that they reflect the main components that were released in the rock, that the electroneutrality in the beaker was provided by some interactions with the reservoir at the exit of the sample, and that the resulting negative species have not been listed.

The full set of chemical species is injected in the algorithm. In Fig. 16, the measured values are in black, the simulations using a

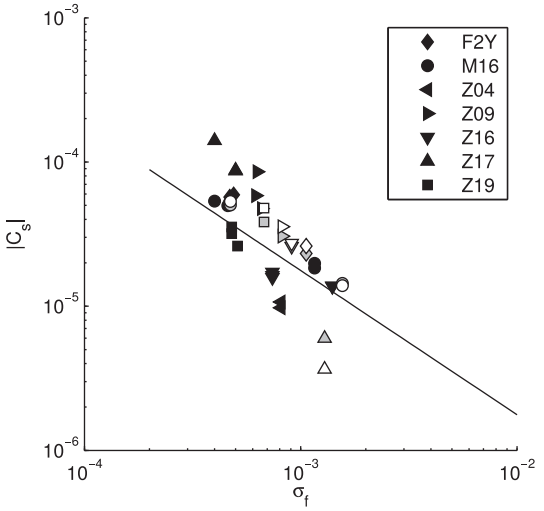

Figure 16. Low salinity domain. (a) EK measurements in black, prediction of eq. (5) with $\zeta = -25$ mV in solid line. Simulations using the chemical analyses in Table 3 with a constant conductivity in grey, simulations with a local conductivity in white ($\zeta = -25$ mV).

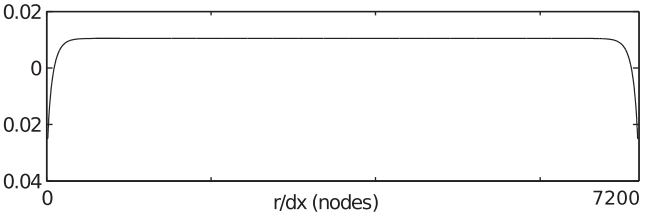

Figure 17. Potential cross-section of the simulation with the chemical composition of F2Y.

classical conductivity are in grey, the simulations with a local conductivity are in white. For each sample, the conductivity calculated from the chemical analysis is greater than the measured conductivity. All the simulations are performed with $\zeta = -25$ mV. Contrary to the previous paragraph, where it was shown that polyvalent counterions lower the streaming potential, the simulated EK coefficients are above the HS equation reference, apart from Z17 which shows a surprising high content of Cl^-. This phenomenon can find an explanation in the diversity of species involved here: for a pure 1:1 electrolyte, eq. (35) creates naturally a zero charge density in the centre of the pore, due to the equal proportion and equal valences of the species. The adjunction of positive species makes this charge density increase, as shown by the computed ρ_e, values. The source term of the Poisson–Boltzmann equation being positive, the potential does not decay to zero far from the rock surface, but reaches a positive constant, as shown in Fig. 17. As referred in Section 3.3, a non-zero potential in the centre of the capillary makes the EK coefficient depart from the HS reference. For a negative potential, as it can be encountered in small channels at low salinities where the condition $d \ll R$ is not satisfied, the EK coefficient is lower than HS. In the present case, the potential created by the massive ion excess is positive, which results in an EK coefficient greater than HS.

However, we can notice that two measurements were made with the samples M16 and Z16. As it could be expected, the conductivity measured at the second measurement is lower than the conductivity measured at the first measurement, since the major part of the species that could be detached from the surface was removed during the first measurement. Yet, the EK coefficients of the first

measurements do not seem affected by their more important positive charge excess. The EK measurements of M16 show the same gap with the HS reference, while the EK measurements of Z16 are similar. If the low salinities generate a massive excess of positive species that is able to increase the EK coefficient as much as what is observed in the simulations, the first EK measurement should be greater than the second one, which is not observed with these two experiments. The simulations show that an overconcentration of cations can increase the EK coefficient, but the experimental data are too scattered and not sufficiently numerous to confirm this hypothesis.

5 DISCUSSION

In this study, the ζ potential is set as a free parameter. It is a rock characteristic that cannot be measured directly, and is always the result of a calculation. The literature reports numerous values of this potential for various fluid-mineral interfaces. A linear correlation between ζ and the logarithm of the counterion concentration was observed (Overbeek 1952; Hunter & Wright 1971). ζ was found to be a decreasing function of C^{∞} due to the diffuse layer contraction with increasing salinity. The main other parameters influencing ζ are the pH, the temperature, the electrolyte and the nature of the mineral. The compilation made by Pride & Morgan (1991) on NaCl/quartz and KCl/quartz data at room temperature and pH = 7 gave

$$\zeta = a + b \log C \tag{36}$$

with $a = 8$ mV and $b = 26$ mV. A complex model for a and b was proposed by Revil *et al.* (1999a), expressing these coefficients as a function of additional parameters. Recently, Luong & Sprik (2014) pointed out that the use of such logarithmic law in the HS equation hardly allows to match the EK coefficient of rocks, and that a constant ζ could be deduced, as in Jouniaux & Ishido (2012) using the compilation of Allègre *et al.* (2010). The same observation is possible in Fig. 18, where the HS equation expressed with eq. (36) passes far above the main cluster of experimental data (grey circles). However, it must be underlined that the simulations of the present work, that mimic the behaviour of the HS equation, are based upon the geometry of a simple capillary, which is a poor representation of realistic geomaterials. Consequently, it seems natural to observe a gap between the HS equation (reproduced by the simulations) and the experimental data, since they do not involve the same petrophysical features. The dots in Fig. 18 report the data from the compilation made by Pride & Morgan (1991) on quartz minerals (Gaudin & Fuerstenau 1955; Li & De Bruyn 1966; Sidorova *et al.* 1975), the data from Ishido & Mizutani (1981) and the data from Lorne *et al.* (1999a) on crushed sand and crushed sandstone. All of them have in common to arise from measurements on ultraclean beads or quartz grains, washed with acid and/or ultrapure water.

Several authors highlighted a link between streaming potentials and the porous structure. Analytical models have demonstrated the EK dependence on grain-size (Revil *et al.* 1999b; Glover *et al.* 2006), pore size and pore throat size (Glover & Déry 2010). In these models the sensitivity to these parameters arise from the surface conductivity term in the HS equation, but it was pointed out by Glover & Déry (2010) that the ζ value itself could be dependent on the grain size, probably due to its role in the positioning of the shear plane. More importantly, the study performed by Lorne *et al.* (1999b) on Fontainebleau sandstones and Villejust quartzite showed that for an electrolyte resistivity $<10^{-2}$ S m^{-1}, the measurements on crushed samples are systematically higher than the measurements on intact rocks. They suggested that the streaming potential is sensitive to the flow path, and that in the case of crushed samples, the hydraulic tortuosity is similar to the electric tortuosity of the network, which is not the case with intact rocks. Considering this, ζ potentials could only be inferred from measurements on crushed samples, due to the fact that intact rocks with lower permeabilities complexify the interaction between the EDL and the flow pattern. The gap between the ζ potential deduced from intact and crushed sandstones observable on their figs 9 and 10, increases with decreasing salinity and is quite comparable to the gap observed between the dots and the grey circles in Fig. 18. This observation supports their hypothesis that the streaming potential is sensitive to the percolation patterns in the rock, and to the petrophysical features that govern the flow. A plausible reason for the increase of the gap with decreasing salinity could be the increase of the thickness of the diffuse layer. In the high salinity domain, the diffuse layer is small, the major portion of velocity field is multiplied by a zero potential, and thus, the velocity changes from one structure to another are barely emphasized. With decreasing salinity, the diffuse layer increases, and enhances a greater portion of the velocity field. Consequently, the velocity changes due to the changes of tortuosity, could be better taken into account. Nonetheless, further work is needed to support the idea that this phenomenon results in a lower EK coefficient with increasing tortuosity.

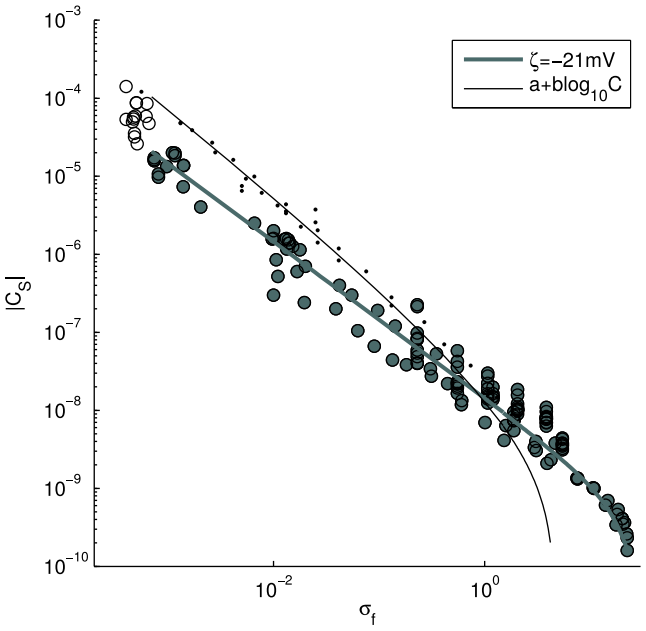

Figure 18. EK coefficient computed using the HS equation and two ζ models compared to measurements. The grey line is calculated using a constant ζ computed with a linear fit, the thin line is the $a + b \log C$ model from Pride & Morgan (1991). The circles are the measurements on sands and sandstones, the dots are the measurements on ultraclean beads or quartz grains.

In addition to the difference of structure between a rock and a grain packing, it can also be debated whether the degree of purity of the material is able to impact the streaming potential, through the unveiling of quartz surface. This question was raised by Lorne *et al.* (1999a) who performed an EK measurement after washing the sample with acid. The ζ potential measured after the cleaning was not found to be much more than the measurement before. However, it is reported in the initial sample preparation procedure that the samples were cleaned by circulating successive reservoirs of pure

water for several hours until the conductivity attained a stable value. It can be inferred from this that the remaining quantity of impurities was already very low. It cannot be excluded, therefore, that the gap between the dots and the grey circles on Fig. 18 could be, at least partly, due to the difference of cleanliness between pure quartz mineral and natural sandstones.

Considering that the parameters impacting the ζ potential are numerous and difficult to control, it is convenient to use an apparent ζ potential that encapsulates all these complex effects inherent to the rock fabric. By setting this parameter constant, with the proper viscosity and permittivity relationships, and with the use of a linear fit combining eq. (5) and eq. (12), a good agreement with the experimental data set (grey data) is found for $\zeta = -21$ mV. Data at low salinity are not included due to their particular behaviour. This value increases to -23 mV with the use of eq. (29) (bulk fluid conductivity), instead of eq. (12). This constant ζ is a practical approximation, allowing to compute realistic EK coefficients on sands and sandstones without knowledge of the rock parameters such as porosity, formation factor or cementation exponent. It can be useful for people interested in studying the streaming potential phenomenon and related geophysical corollaries per se, without sensitivity to detailed petrophysical features, like in the current study.

The measurements at high salinity performed by Jaafar *et al.* (2009) and Vinogradov *et al.* (2010) showed that the EK coefficient was decreasing less than the prediction using eq. (36) in the HS equation. The ζ potentials that they calculate from their measurements appear to be constant or slightly increasing in this range of salinity. Their interpretation was that contrary to the Boltzmann theory that describes ions as point charges, real ions have an incompressible thickness, that prevents the diffuse layer from decreasing endlessly with increasing concentration. This incompressible thickness leads to a floor value for the ζ potential. However, the local decrease of the permittivity in the vicinity of the mineral can decrease the EK coefficient, and such decrease would require an increasing ζ with increasing salinity instead of a constant ζ (Glover *et al.* 2012). The current simulations show that the local permittivity does decrease the EK coefficient, but not in a significant manner. The model for local viscosity provided by Pride & Morgan (1991) is of the same type, and lets expect the same order of impact. These results do not tip the balance towards a necessary increase of ζ in the high salinity domain, due to local permittivity and viscoelectric effects.

At very low salinities, after equilibrium with the rock, the pore fluid conductivity shows an increase compared to its initial value. This difference between the initial conductivity and the conductivity at the moment of the streaming potential measurement was pointed out by Walker *et al.* (2014), who showed that this effect must be taken into account for concentrations $<10^{-3}$ mol L^{-1}. The chemical analyses of the expelled fluid show the release of a variety of species in proportion comparable to the amount of initial species. In these cases, the deduced ζ potentials may be disturbed by the presence of anomalous species. For a given ζ, the simulations show that a massive excess of positive species is able to increase the EK coefficient. The experiments performed on two separate days do not confirm this trend, but it is an interesting research prospect that could deserve further investigations.

The key point of this article is the derivation of a model for the pore fluid conductivity, that derives both from the fluid and from the remote effect of the mineral surface charge. It is known that the species density depends on the potential experienced locally by the ions. In the middle of the pore, if $d \ll R$, the potential is zero, and the species distribution is similar to what can be observed out of the capillary. In the vicinity of the mineral the potential increases up to the value fixed by ζ, the quantity of negative ions decreases, and the quantity of positive ions increases. This increase is correlated to the magnitude of ζ: the higher ζ, the greater the increase. This excess of positive species generates a local enhancement of the fluid conductivity that impacts the global streaming current. These local variations of the fluid conductivity have been quantified through the derivation of a bulk fluid conductivity model, both numerically and analytically. These expressions allow to consider the species distribution that really takes place in the porous medium, which is not possible with the classical formulation of the electrolyte conductivity.

The advantage of the numerical expression upon the analytical one is that its derivation is not based on the Debye–Hückel approximation. This approximation makes consider, in the vicinity of the mineral, a potential that is greater than the potential really experienced by the ions. Without this approximation, the sensitivity of the conductivity to the ζ variations is modified. With a larger conductivity, a larger ζ is needed to reach the same EK values, and the ζ potentials derived from experiments using the HS equation appears to be in serious error. In the low salinity domain, the real potential of the shear plane could be twice the value given by eq. (36). Unfortunately, this approximation is hard to avoid, due to lack of solution for the fully non-linear form of the Poisson–Boltzmann equation in general conditions. It can also be argued that the error that is made in one sense by deriving the ζ potential, is made in the opposite sense by reinjecting the ζ potential in the HS equation, which amounts to a null operation. But the sensitivity to Debye–Hückel approximation is probably not the same for all the types of electrolyte.

Using the analytical expression, the impact of a non-monovalent counterion has been quantified. The increase of the valence increases the thickness of the diffuse layer, as well as the magnitude of the local conductivity enhancement. Consequently, all the ζ potentials of non-monovalent counterions that are deduced from EK measurements through the HS equation are likely to be underestimated. The lower EK coefficients of non-monovalent species are (at least partly) due to the increase of bulk fluid conductivity with increasing valence. The classical conductivity does not allow to comprehend these local variations, and hence the sensitivity to the valence. The real ζ potentials of non-monovalent species are likely to be not as low as the ones derived using the HS equation (Watillon & De Backer 1970; Lorne *et al.* 1999a; Gu & Li 2000), especially at low concentration, where ζ reaches a strong magnitude.

6 CONCLUSIONS

A compilation of EK coefficients on sands and sandstones showing anomalous behaviours at high and low salinities was compared to simulations and analytical solutions. The conclusions of this article are the following: (i) A coupled LB algorithm is implemented and shown able to model streaming potentials properly. (ii) The salinity dependence of permittivity and viscosity must be taken into account in the high salinity domain (typically when $C^{\infty,m} > 0.1$ mol L^{-1}). The local variations of these quantities increase with increasing salinity, but remain negligible. (iii) The low salinities generate a diversity of species that complexifies the interpretation of ζ potentials in this domain, in the case of natural materials. This release of chemical species could be responsible for the apparent increase of the EK coefficient. (iv) Considering intact rocks, the salinity dependence of the ζ potential appears blurred, and a constant approximation is proposed. (v) Overall, a model for bulk fluid electrical

conductivity is derived. The numerically derived expression allows to break free from the Debye–Hückel approximation, whereas the analytical expression is valid whatever the type of the species. This model allows to consider the change of ionic distribution at the vicinity of the rock mineral, as well as the nature of the electrolyte, which is particularly important at low concentration, and in the presence of a polyvalent counterion. Using this model, we can observe that the ζ potentials of polyvalent cations are usually underestimated, due to the lack of consideration of conductivity enhancement with increasing valence.

ACKNOWLEDGEMENTS

The measurements of this study were performed by Laurence Jouniaux and Maria Zamora, and the solutions were analysed by Nicole Catel at the laboratory of Ecole Normale Superieure, Paris, 2001. This work benefited from the support of the University of Strasbourg, the CNRS, NEEDS MIPOR and the Direction Informatique (Pôle HPC) of the University of Strasbourg. We thank Damien Daval, Damien Jougnot, Jean-Christophe Géminard, Eirik Flekkøy and Steve Pride for valuable discussions.

REFERENCES

Ahmad, M.U., 1964. A laboratory study of streaming potentials, *Geophys. Prospect.,* **12**(1), 49–64.

Alkafeef, S. & Alajmi, A., 2006. Streaming potentials and conductivities of reservoir rock cores in aqueous and non-aqueous liquids, *Colloids Surf. A,* **289,** 141–148.

Allègre, V., Jouniaux, L., Lehmann, F. & Sailhac, P., 2010. Streaming Potential dependence on water-content in fontainebleau sand, *Geophys. J. Int.,* **182,** 1248–1266.

Booth, F., 1951. The dielectric constant of water and the saturation effect, *J. Chem. Phys.,* **19**(4), 391–394.

Bouchaud, E., 1997. Scaling properties of cracks, *J. Phys.: Condens. Matter.,* **9**(21), 4319–4344.

Bourbie, T. & Zinszner, B., 1985. Hydraulic and acoustic properties as a function of porosity in Fontainebleau sandstone, *J. geophys. Res.,* **90**(B13), 11 524–11 532.

Briggs, D., 1928. The determination of the zeta-potential on cellulose-a method, *J. Phys. Chem.,* **32**(5), 641–675.

Chai, Z. & Shi, B., 2008. A novel lattice Boltzmann model for the Poisson equation, *Appl. Math. Modelling,* **32,** 2050–2058.

Chopard, B. & Droz, M., 1998. *Cellular Automata Modeling of Physical Systems,* Cambridge Univ. Press.

Flekkøy, E.G., 1993. Lattice Bhatnagar-Gross-Krook models for miscible fluids, *Phys. Rev. E,* **47,** 4247–4257.

Gao, Y. & Hu, H., 2010. Seismoelectromagnetic waves radiated by a double couple source in a saturated porous medium, *Geophys. J. Int.,* **181,** 873–896.

Gao, Y., Chen, X., Hu, H. & Zhang, J., 2013. Early electromagnetic waves from earthquake rupturing:ii validation and numerical experiments, *Geophys. J. Int.,* **192**(3), 1308–1323.

Gaudin, A.M. & Fuerstenau, D.W., 1955. Streaming potential studies: quartz flotation with cationic collectors, *Min. Eng., Trans. AIME,* **202,** 66–72.

Glover, P. & Déry, N., 2010. Streaming potential coupling coefficient of quartz glass bead packs: dependence on grain diameter, pore size, and pore throat radius, *Geophysics,* **75,** F225–F241.

Glover, P.W.J., Zadjali, I.I. & Frew, K.A., 2006. Permeability prediction from MICP and NMR data using an electrokinetic approach, *Geophysics,* **71,** F49–F60.

Glover, P.W.J., Walker, E. & Jackson, M.D., 2012. Streaming-potential coefficient of reservoir rock: a theoretical model, *Geophys. J. Int.,* **77**(2), D17–D43.

Grahame, D.C., 1947. The electrical double layer and the theory of electrocapillarity, *Chem. Rev.,* **41**(3), 441–501.

Gu, Y. & Li, D., 2000. The ζ-potential of glass surface in contact with aqueous solutions, *J. Colloid Interface Sci.,* **226**(2), 328–339.

Guichet, X., Jouniaux, L. & Pozzi, J.-P., 2003. Streaming potential of a sand column in partial saturation conditions, *J. geophys. Res.,* **108**(B3), doi:10.1029/2001JB001517.

Guichet, X., Jouniaux, L. & Catel, N., 2006. Modification of streaming potential by precipitation of calcite in a sand–water system: laboratory measurements in the ph range from 4 to 12, *Geophys. J. Int.,* **166**(1), 445–460.

Guo, Z., Shi, B. & Zheng, C., 2002. A coupled lattice BGK model for the boussinesq equations, *Int. J. Numer. Methods Fluids,* **39**(4), 325–342.

Hunter, R.J., 1981. *Zeta Potential in Colloid Science: Principles and Applications,* Academic Press Inc.

Hunter, R.J. & Wright, H.J.L., 1971. The dependence of electrokinetic potential on concentration of electrolyte, *J. Colloid Interface Sci.,* **37**(3), 564–580.

Hunter, R.J., 1966. The interpretation of electrokinetic potentials, *J. Colloid Interface Sci.,* **22**(3), 231–239.

Ishido, T. & Mizutani, H., 1981. Experimental and theoretical basis of electrokinetic phenomena in rock-water systems and its applications to geophysics, *J. geophys. Res.,* **86**(B3), 1763–1775.

Jaafar, M.Z., Vinogradov, J. & Jackson, M.D., 2009. Measurement of streaming potential coupling coefficient in sandstones saturated with high salinity NaCl brine, *Geophys. Res. Lett.,* **36**(21), doi:10.1029/2009GL040549.

Jackson, M.D. & Leinov, E., 2012. On the validity of the "thin" and "thick" double-layer assumptions when calculating streaming currents in porous media, *Int. J. Geophys.,* doi:10.1155/2012/897807.

Jouniaux, L. & Ishido, T., 2012. Electrokinetics in Earth Sciences: a tutorial, *Int. J. Geophysics,* doi:10.1155/2012/286107.

Jouniaux, L. & Pozzi, J.-P., 1997. Laboratory measurements anomalous 0.1–0.5 hz streaming potential under geochemical changes: Implications for electrotelluric precursors to earthquakes, *J. geophys. Res.,* **102**(B7), 15 335–15 343.

Jouniaux, L., Lallemant, S. & Pozzi, J.-P., 1994. Changes in the permeability, streaming potential and resistivity of a claystone from the Nankai prism under stress, *Geophys. Res. Lett.,* **21,** 149–152.

Jouniaux, L., Pozzi, J.-P., Berthier, J. & Massé, P., 1999. Detection of fluid flow variations at the Nankai trough by electric and magnetic measurements in boreholes or at the seafloor, *J. geophys. Res.,* **104,** 29 293–29 309.

Jouniaux, L., Bernard, M.-L., Zamora, M. & Pozzi, J.-P., 2000. Streaming potential in volcanic rocks from Mount Peleé, *J. geophys. Res.,* **105,** 8391–8401.

Kirby, B.J. & Hasselbrink, E.F., 2004. Zeta potential of microfluidic substrates: 1. theory, experimental techniques, and effects on separations, *Electrophoresis,* **25**(2), 187–202.

Leroy, P., Revil, A., Kemna, A., Cosenza, P. & Ghorbani, A., 2008. Complex conductivity of water-saturated packs of glass beads, *J. Colloid Interface Sci.,* **321**(1), 103–117.

Levy, A., Andelman, D. & Orland, H., 2012. Dielectric constant of ionic solutions: A field-theory approach, *Phys. Rev. Lett.,* **108**(22), doi:10.1103/PhysRevLett.108.227801.

Li, H. & De Bruyn, P., 1966. Electrokinetic and adsorption studies on quartz, *Surf. Sci.,* **5**(2), 203–220.

Li, S., Pengra, D. & Wong, P., 1995. Onsager's reciprocal relation and the hydraulic permeability of porous media, *Phys. Rev. E,* **51**(6), 5748–5751.

Lide, D.R., 2005. *Handbook of Chemistry and Physics,* CRC Press.

Lorne, B., Perrier, F. & Avouac, J.-P., 1999a. Streaming potential measurements. 1. Properties of the electrical double layer from crushed rock samples, *J. geophys. Res.,* **104**(B8), 17 857–17 877.

Lorne, B., Perrier, F. & Avouac, J.-P., 1999b. Streaming potential measurements. 2. relationship between electrical and hydraulic flow patterns from rocks samples during deformations, *J. geophys. Res.,* **104**(B8), 17 879–17 896.

Luong, D.T. & Sprik, R., 2014. Examination of a theoretical model of streaming potential coupling coefficient, *Int. J. Geophys.,* doi:10.1155/2014/471819.

Maineult, A., Jouniaux, L. & Bernabé, Y., 2006. Influence of the mineralogical composition on the self-potential response to advection of KCl concentration fronts through sand, *Geophys. Res. Lett.,* (33), L24311, doi:10.1029/2006GL028048.

Mauri, G., Williams-Jones, G. & Saracco, G., 2010. Depth determinations of shallow hydrothermal system by self-potential and multi-scale wavelet tomography, *J. Volcanol. Geotherm. Res.,* **191,** 233–244.

Misztal, M.K., Hernandez-Garcia, A., Matin, R., Sørensen, H.O. & Mathiesen, J., 2015. Detailed analysis of the lattice Boltzmann method on unstructured grids, *J. Comput. Phys.,* **297,** 316–339.

Morgan, F.D., Williams, E.R. & Madden, T.R., 1989. Streaming potential properties of westerly granite with applications, *J. geophys. Res.,* **94**(B9), 12 449–12 461.

Neuville, A., Toussaint, R. & Schmittbuhl, J., 2010. Hydrothermal coupling in a self-affine rough fracture, *Phys. Rev. E,* **82,** 036317, doi:10.1103/PhysRevE.82.036317.

Neuville, A., Flekkøy, E.G. & Toussaint, R., 2013. Influence of asperities on fluid and thermal flow in a fracture: A coupled lattice Boltzmann study, *J. geophys. Res.,* **118,** 3394–3407.

Obliger, A., Duvail, M., Jardat, M., Coelho, D., Békri, S. & Rotenberg, B., 2013. Numerical homogenization of electrokinetic equations in porous media using lattice-boltzmann simulations, *Phys. Rev. E,* **88,** 013019, doi:10.1103/PhysRevE.88.013019.

Ogilvy, A.A., Ayed, M.A. & Bogoslovsky, V.A., 1969. Geophysical studies of water leakages from reservoirs, *Geophys. Prospect.,* **17**(1), 36–62.

Overbeek, J.T.G., 1952. Electrochemistry of the double layer, in *Colloid Science, Irreversible Systems,* vol. 1, pp. 115–193, ed. Kyuyt, H.R., Elsevier.

Pengra, D.B., Li, S.X. & Wong, P.Z., 1999. Determination of rock properties by low frequency ac electrokinetics, *J. geophys. Res.,* **104**(B12), 29 485–29 508.

Perrier, F. & Froidefond, T., 2003. Electrical conductivity and streaming potential coefficient in a moderately alkaline lava series, *Earth planet. Sci. Lett.,* **210,** 351–363.

Pozzi, J.-P. & Jouniaux, L., 1994. Electrical effects of fluid circulation in sediments and seismic prediction, *C.R. Acad. Sci., Paris II,* **318**(1), 73–77.

Press, W.H., 2007. *Numerical Recipes 3rd edition: The Art of Scientific Computing*, Cambridge Univ. Press.

Pride, S., 1994. Governing equations for the coupled electromagnetics and acoustics of porous media, *Phys. Rev. B,* **50,** 15 678–15 696.

Pride, S. & Morgan, F.D., 1991. Electrokinetic dissipation induced by seismic waves, *Geophysics,* **56**(7), 914–925.

Revil, A. & Glover, P., 1998. Nature of surface electrical conductivity in natural sands, sandstones, and clays, *Geophys. Res. Lett.,* **25**(5), 691–694.

Revil, A., Pezard, P.A. & Glover, P.W.J., 1999a. Streaming potential in porous media 1. Theory of the zeta-potential, *J. geophys. Res.,* **104,** 20 021–20 031.

Revil, A., Schwaeger, H., Cathles, L.M., III & Manhardt, P.D., 1999b. Streaming potential in porous media: 2. Theory and application to geothermal systems, *J. geophys. Res.,* **104**(B9), 20 033–20 048.

Rolland, A., Toussaint, R., Baud, P., Conil, N. & Landrein, P., 2014. Morphological analysis of stylolites for paleostress estimation in limestones, *Int. J. Rock Mech. Min. Sci.,* **67,** 212–225.

Rothman, D.H. & Zaleski, S., 1997. *Lattice-Gas Cellular Automata,* Cambridge Univ. Press.

Ruffet, C., Guéguen, Y. & Darot, M., 1991. Complex conductivity and fractal microstructures, *Geophysics,* **56,** 758–768.

Rutgers, A., 1940. Streaming effects and surface conduction. streaming potentials and surface conductance, *Trans. Faraday Soc.,* **35,** 69–80.

Sailhac, P. & Marquis, G., 2001. Analytic potentials for the forward and inverse modeling of sp anomalies caused by subsurface fluid flow, *Geophys. Res. Lett.,* **28,** 1851–1854.

Saracco, G., Labazuy, P. & Moreau, F., 2004. Localization of self-potential sources in volcano-electric effect with complex continuous wavelet transform and electrical tomography methods for an active volcano, *Geophys. Res. Lett.,* (31), L12610, doi:10.1029/2004GL019554.

Saunders, J.H., Jackson, M.D. & Pain, C.C., 2008. Fluid flow monitoring in oilfields using downhole measurements of electrokinetic potential, *Geophysics,* **73,** E165–E180.

Sen, P. & Goode, P., 1992. Influence of temperature on electrical conductivity on shaly sands, *Geophysics,* **57,** 89–96.

Sidorova, M.P., Fazylova, M. & Fridrikhsberg, D.A., 1975. Electrokinetic studies of some model systems: quartz-electrolyte solutions, in *Proc. Inter. Conf. Colloid Surf. Sci.,* ed. Wolfram, E., Elsevier Science Publ. Co., Inc.

Vinogradov, J. & Jackson, M., 2011. Multiphase streaming potential in sandstones saturated with gas/brine and oil/brine during drainage and imbibition, *Geophys. Res. Lett.,* **38,** L01301, doi:10.1029/2010GL045726.

Vinogradov, J., Jaafar, M.Z. & Jackson, M.D., 2010. Measurement of streaming potential coupling coefficient in sandstones saturated with natural and artificial brines at high salinity, *J. geophys. Res.,* **115**(B12), doi:10.1029/2010JB007593.

Walker, E., Glover, P.W.J. & Ruel, J., 2014. A transient method for measuring the DC streaming potential coefficient of porous and fractured rocks, *J. geophys. Res.,* **119**(2), 957–970.

Wang, M. & Kang, Q., 2010. Modeling electrokinetic flows in microchannels using coupled lattice boltzmann methods, *J. Comput. Phys.,* **229,** 728–744.

Wang, J. & Hu, H., 2012. The determination of electrokinetic coupling coefficient and zeta potential of rock samples by electrokinetic measurements, *Adv. Mater. Res.,* **516–517,** 1870–1873.

Wang, J., Hu, H., Guan, W. & Li, H., 2015. Electrokinetic experimental study on saturated rock samples: zeta potential and surface conductance, *Geophys. J. Int.,* **201**(2), 869–877.

Warden, S., Garambois, S., Jouniaux, L., Brito, D., Sailhac, P. & Bordes, C., 2013. Seismoelectric wave propagation numerical modeling in partially saturated materials, *Geophys. J. Int.,* **194,** 1498–1513.

Watillon, A. & De Backer, R., 1970. Potentiel d'écoulement, courant d'écoulement et conductance de surface à l'interface eau-verre, *J. Electroanal. Chem. Interfacial Electrochem.,* **25**(2), 181–196.

Werner, C., Körber, H., Zimmermann, R., Dukhin, S. & Jacobasch, H.-J., 1998. Extended electrokinetic characterization of flat solid surfaces, *J. Colloid Interface Sci.,* **208**(1), 329–346.

Wolf-Gladrow, D.A., 2005. *Lattice Gas Cellular Automata and Lattice Boltzmann Models —An Introduction,* Springer.

Zyserman, F., Jouniaux, L., Warden, S. & Garambois, S., 2015. Borehole seismoelectric logging using a shear-wave source: possible application to CO_2 disposal?, *Int. J. Greenhouse Gas Control,* **33,** 82–102.

APPENDIX: ROUGH SURFACE

The current model assumes that the fluid–rock interface is perfectly planar, but real porous surfaces show anfractuosities. It is demonstrated that these anfractuosities are able to impact the flow (e.g. Bouchaud 1997). In this appendix, the tests are performed with synthetic rough surfaces. The rough surfaces are generated using the same procedure as Press *et al.* (1992), Neuville *et al.* (2010) and Rolland *et al.* (2014). The capillary aperture is adapted to the Debye length so that $2R/d = 120$. The flow is simulated on a 200 × 250 matrix, so as to get a significant portion of surface. Using the criterion $d/dx = 60$ (see Section 3.3), the electrical potential is simulated on a 5755 × 7200 grid, which represents a heavy computation. This problem could be lightened through the use of unstructured LB simulations that couple LB methods with finite volume schemes (Misztal *et al.* 2015). The maximum thickness of the asperities is denoted by H. Fig. A1 shows the velocity field, electrical potential and electrical field in a situation where H amounts to 4 per cent of the diameter of the channel, giving $H/d = 4.8$, and in a situation where H reaches 8 per cent of the diameter, giving $H/d = 9.6$. In both cases, the asperities lower the EK coefficient compared to the

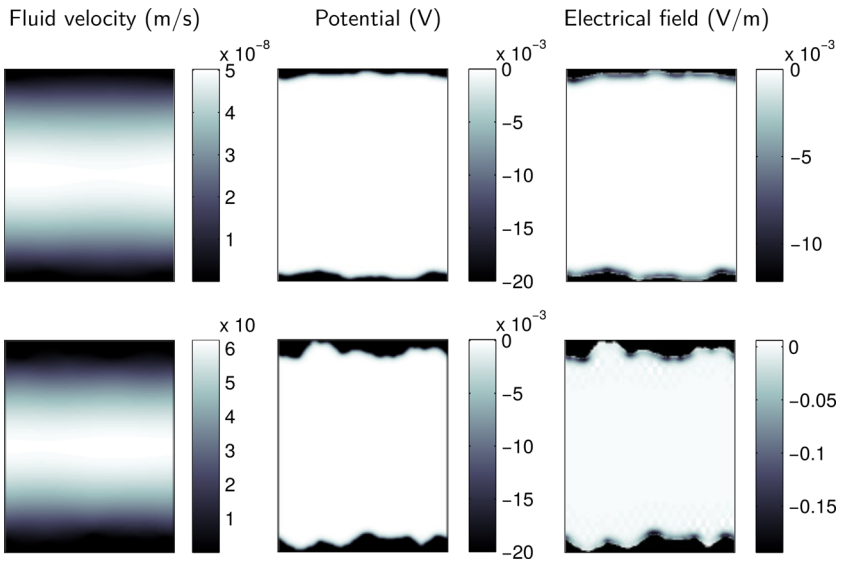

Figure A1. Simulated velocity, potential and electrical field in a channel with asperities. First row: $H/d = 4.8$; second row: $H/d = 9.6$.

planar situation, even if some instabilities have to be reported in the computation of the potential with increasing surface roughness. The anfractuosities make the zero fluid speed areas increase, whereas the potential remains in the same proportion. The difference with HS amounts to 8 per cent for $H/d = 4.8$, and reaches 25 per cent for $H/d = 9.6$. This would mean that for a given geometry, the decrease of the EK coefficient would be more important for thin diffuse layers as encountered at high salinities. However, such a deviation needs the support of a sufficiently high H to be observable, and further work is needed to determine if this effect is not overwhelmed by other features of the porous complexity such as the grain sizes or the pore and pore throat diameters (Leroy *et al.* 2008).